Black Marble User Guide Version 1.0

Product's Principal Investigator:

Dr. Miguel O. Román

List of Contributors:

Zhuosen Wang, Ranjay Shrestha, Tian Yao, and Virginia Kalb

March 2019

Contents

1 Introduction 1
2 Algorithm 2
2.1 Overview of the Algorithm 2
2.2 Atmospheric Correction 3
2.3 BRDF Correction 4
2.3 Seasonal Vegetation Correction 5
3 Data Product Formats 6
3.1 Metadata 6
3.2 Filenames 7
3.3 Projection 7
4. Product generation 8
5 Scientific Data Sets (SDSs) from VNP46 Product Suite 10
5.1 The VNP46A1 Daily At-sensor TOA Nighttime Radiance Product 10
5.2 The VNP46A2 Daily Moonlight-adjusted Nighttime Lights (NTL) Product 15
5.3 Examples of the VNP46 Product Suite 16
6 Evaluation and Validation of the Product 18
7 Data Archives 21
8 Data Usage and Citation Policies 21
9 Contact Information 21
10 Related Publications 21
References 23
Appendix A: Metadata (Attributes) in VNP46A1 Product 33
Appendix B: Metadata (Attributes) in VNP46A2 Product 36

List of Figures

Figure 1 Overview of NASA's Black Marble retrieval strategy (*cf.*, Equation 1). 4

Figure 2 The Suomi-NPP VIIRS linear latitude/longitude (or geographic) grid consists of 460 non-overlapping Land tiles which measure approximately 10°×10° region. 8

Figure 3 Algorithm processing cycle and ancillary parameters used by NASA's Black Marble product suite (VNP46). 9

Figure 4 VNP46 product suite components for a 10° × 10° Level 3 tile over France and the Balearic Sea region (h18v04; DOY 2015-091). 17

Figure 5 VNP46 product suite components for a 10° × 10° Level 3 tile over Sweden and Finland (h20v02; DOY 2013-080). 18

Figure 6 The NTL radiance at the Pitahaya farmland site in Cabo Rojo, PR on 1st, 2nd and 3rd March 2017. 20

List of Tables

Table 1 Black Marble VNP46A1 product input files.....8
Table 2 Black Marble VNP46A2 product input files.....9
Table 3 Scientific datasets included in the VNP46A1 daily at-sensor TOA nighttime radiance product..12
Table 4 Value of QF_Cloud_Mask in the VNP46A1 product.....14
Table 5 Value of QF_DNB and QF of VIIRS band M10/11/12/13/15/16 in the VNP46A1 product.....14
Table 6 Scientific datasets included in VNP46A2 daily moonlight-adjusted NTL product.....15
Table 7 Values of the Mandatory_Quality_Flag in VNP46A2 product.....16
Table 8 Values of the Snow_Flag in VNP46A2 product. 16
Table 9 Key performance metrics established for NASA's Black Marble product suite. 19

Acryonyms

AERONET	Aerosol Robotic Network
AOD	Aerosol Optical Depth
BRDF	Bidirectional Reflectance Distribution Function
BRF	Bidirectional Reflectance Factor
DMSP	Defense Meteorological Satellite Program
DNB	Day/Night Band
EOS	Earth Observing System
GEO	Group on Earth Observations
GIS	Geographic Information System
HAM	Half-angle Mirror
HDF-EOS	Hierarchical Data Format - Earth Observing System
IDPS	Interface Data Processing Segment
IR	Infrared
L1B	Level-1 B
L2G	Level-2 Gridded
LAI	Leaf Area Index
LANCE	The Land, Atmosphere Near-real-time Capability for EOS
LZA	Lunar Zenith Angle
JPSS	Joint Polar Satellite System
NASA	National Aeronautics and Space Administration
NBAR	Nadir BRDF-Adjusted Reflectance
NCEP	National Centers for Environmental Prediction
NDVI	Normalized Difference Vegetation Index
NDSI	Normalized Difference Snow Index
NIR	Near-infrared
NRT	Near-Real-Time
NTL	Nighttime Lights
Pgap	Gap Fraction Probability
PGE	Product Generated Executable
PRWGLP	Puerto Rico's Working Group on Light Pollution
QA	Quality Assurance
QF	Quality Flag
RTA	Rotating Telescope Assembly
SDS	Scientific Data Set
SIPS	Science Investigator-led Processing System
S-NPP	Suomi National Polar-orbiting Platform
TOA	Top of Atmosphere
UTC	Coordinated Universal Time
VCM	VIIRS Cloud Mask
VCST	VIIRS Calibration Support Team
VIIRS	Visible Infrared Imaging Radiometer Suite
VNP09	VIIRS Surface Reflectance product
VNP46	NASA's Black Marble nighttime lights product suite
VNP46A1	Daily at-sensor TOA nighttime radiance product
VNP46A2	Daily moonlight-adjusted nighttime lights product

1 Introduction

The Day/Night Band (DNB) sensor of the Visible Infrared Imaging Radiometer Suite (VIIRS), on board the Suomi-National Polar-orbiting Partnership (S-NPP) and Joint Polar Satellite System (JPSS) satellite platforms, provide global daily measurements of nocturnal visible and near-infrared (NIR) light that are suitable for Earth system science and applications studies. The VIIRS DNB's ultra-sensitivity in lowlight conditions allows us to generate new science-quality nighttime products as a result of significant improvements to sensor resolution and calibration compared to those previously provided by the Defense Meteorological Satellite Program's (DMSP) nighttime lights imagery. These improvements allow us to better monitor both the magnitude and signature of nighttime phenomena, and anthropogenic sources of light emissions.

Since the launch of the S-NPP satellite in 2011, multiple studies have used the VIIRS DNB as the primary data source in a wide range of study topics. They include: (1) feature extraction techniques to detect severe weather impacts to urban infrastructure (Cao et al., 2013; Cole et al., 2017; Mann et al., 2016; Molthan and Jedlovec, 2013); (2) detection of sub-pixel scale features, e.g., fires (Polivka et al., 2016), shipping vessels (Asanuma et al., 2016; Elvidge et al., 2015; Straka et al., 2015), lightning flashes (Bankert et al., 2011), surface oil slicks (Hu et al., 2015), and gas flares (Elvidge et al., 2015; Liu et al., 2017, Liu et al., 2017); and (3) techniques for monitoring nighttime atmospheric optical properties, including clouds (Minnis et al., 2016; Walther et al., 2013), aerosols (Johnson et al., 2013; McHardy et al., 2015), particulate matter (Wang et al., 2016), and gravity waves in the upper atmosphere via nightglow (Miller et al., 2015).

As with early research that utilized the DMSP 's Operational Line Scanner (OLS) (Huang et al., 2014), recent studies using the VIIRS DNB have employed statistical analyses and correlation discovery methods to confirm established empirical relationships with a wide range of human-linked patterns and processes. They include socioeconomic variables (Chen and Nordhaus, 2015; Chen et al., 2015; Levin and Zhang, 2017; Li et al., 2013; Ma et al., 2014; Shi et al., 2014; Yu et al., 2015), as well as changes driven by urban expansion (Guo et al., 2015; Sharma et al., 2016; Shi et al., 2014), energy use (Coscieme et al., 2014; Román and Stokes, 2015), and carbon emissions (Oda et al., 2017; Ou et al., 2015).

To realize the full potential of the VIIRS DNB time-series record, NASA has developed a new suite of standard products that represents the current state-of-the-art in nighttime lights (NTL) applications, the NASA’s Black Marble product suite (VNP46). Based on VIIRS DNB data, this product suite, at 500-m resolution, is available from January 2012 through the present. The VNP46 product suite is being

processed on a daily basis within 3-5 hours of acquisition, which enables both near- real-time uses and long-term monitoring applications. The VNP46 product suite includes the daily at-sensor top of atmosphere (TOA) nighttime radiance product (VNP46A1), and the daily moonlight-adjusted NTL product (VNP46A2). The retrieval algorithm, developed and implemented for routine global processing at NASA's Land Science Investigator-led Processing System (SIPS), utilizes all high-quality, cloud-free, atmospheric-, terrain-, vegetation-, snow-, lunar-, and stray light-corrected radiance to estimate daily NTL and other intrinsic surface optical properties. The VIIRS Black Marble product has been used for global mapping of human activity patterns, such as tracking shipping and fishing vessels, gas flaring, in addition to their application to humanitarian efforts, such as assessment of conflict-associated demographic changes and mapping impoverishment.

This user guide provides an overview of NASA's new VIIRS Level-3 Black Marble nighttime lights product suite (VNP46) to users. This document describes the theoretical basis for the algorithms, the operational processing, evaluation and validation of the product, and how to access the product. Additional details are available in related publications within section 10.

2 Algorithm

2.1 Overview of the Algorithm

NASA's operational Black Marble product suite (VNP46) ingests multiple-source input datasets and ancillary data to output the highest quality pixel-based estimates of NTL. These NTL estimates are accompanied by pixel-level quality flags. The principal features of the algorithm are summarized in the following sections. More details of the algorithm are available in related publications in section 10.

The NASA Black Marble algorithm produces cloud-free imagery that has been corrected for atmospheric, terrain, lunar BRDF, thermal, and straylight effects. The corrected nighttime radiance, resulting in a superior retrieval of nighttime lights at short time scales and a reduction in background noise, enables quantitative detection and analyses of daily, seasonal and annual variations. Key algorithm enhancements include: (1) lunar irradiance modeling to resolve non-linear changes in phase and libration; (2) vector radiative transfer and lunar bidirectional surface anisotropic reflectance modeling to correct for atmospheric and bidirectional reflectance distribution function (BRDF) effects; (3) geometric-optical and canopy radiative transfer modeling to account for seasonal variations in NTL; and (4) temporal gap-filling to reduce persistent data gaps.

2.2 Atmospheric Correction

NASA's Black Marble retrieval strategy combines daytime VIIRS DNB surface reflectance, BRDF, surface albedo, nadir BRDF-adjusted reflectance (NBAR), and lunar irradiance values to minimize the biases caused by extraneous artifacts in the VIIRS NTL time-series record.

Using this novel "turning off the Moon" approach, illustrated in Figure 1, the surface upward radiance from artificial light emissions, L_{NTL} [units of nWatts·cm^{-2}·sr^{-1}], can be extracted from at-sensor nighttime radiance at TOA, L_{DNB}, using the following equation:

$$L_{NTL} = \left[\left(\frac{L_{DNB}-L_{path}}{T_{\uparrow}(\tau\theta_v)}\right)(1-a(\theta_m)\rho_a) - L_m T_{\downarrow}(\tau\theta_v)\right] / P_{\uparrow}(\theta_v) \quad (1)$$

where L_{path} is the nighttime path radiance (*i.e.*, the radiance generated by scattering within the atmosphere), and $a(\theta_m)$ is the VIIRS-derived actual (or blue-sky) surface albedo; incorporating the directional influence of sky radiance and multiple scattering effects between the ground and the atmosphere (Román et al., 2010). For the latter, a snow albedo retrieval scheme is used if the VIIRS current day snow status flag is activated (Klein and Stroeve, 2002; Liu et al., 2017, Liu et al., 2017; Moustafa et al., 2017; Wang et al., 2012). $P_{\uparrow}(\theta_v)$ is the probability of the upward transmission of NTL emissions through the urban vegetation canopy, defined in Equation 4. The atmospheric backscatter is given by ρ_a, and $T_{\downarrow}(\tau,\theta_v)$ and $T_{\uparrow}(\tau,\theta_v)$ are the total transmittance (including direct and diffuse radiation) along the lunar-ground and ground-sensor paths, respectively. The latter two are a function of view-illumination geometry and the total atmospheric column optical depth (τ) due to mixed gases, water vapor, and aerosol particles. The retrieval uses a modified algorithm based on the VIIRS Surface Reflectance product (VNP09) to estimate the values of L_{path}, ρ_a, $T_{\downarrow}(\tau,\theta_v)$, and $T_{\uparrow}(\tau,\theta_v)$ for a given set of surface and atmospheric conditions (Roger et al., 2016; Skakun et al., 2018). Additional input datasets include the standard VIIRS Cloud Mask (VCM[1]) (Kopp et al., 2014), atmospheric profiles obtained from the National Centers for Environmental Prediction (NCEP) model (*i.e.*, water vapor, ozone, and surface pressure) (Moorthi et al., 2001), and the VIIRS aerosol model[2] combined with daytime-to-daytime averaged aerosol optical depth (AOD) at 0.550 µm to extrapolate the nighttime AOD.

[1] Refers to the VIIRS Land Cloud Mask Intermediate product generated at Land SIPS using its variation of the IDPS version of the VCM algorithm.

[2] Refers to the VIIRS Land Aerosol intermediate product generated at Land SIPS using its variation of the IDPS version of the Aerosol IP algorithm.

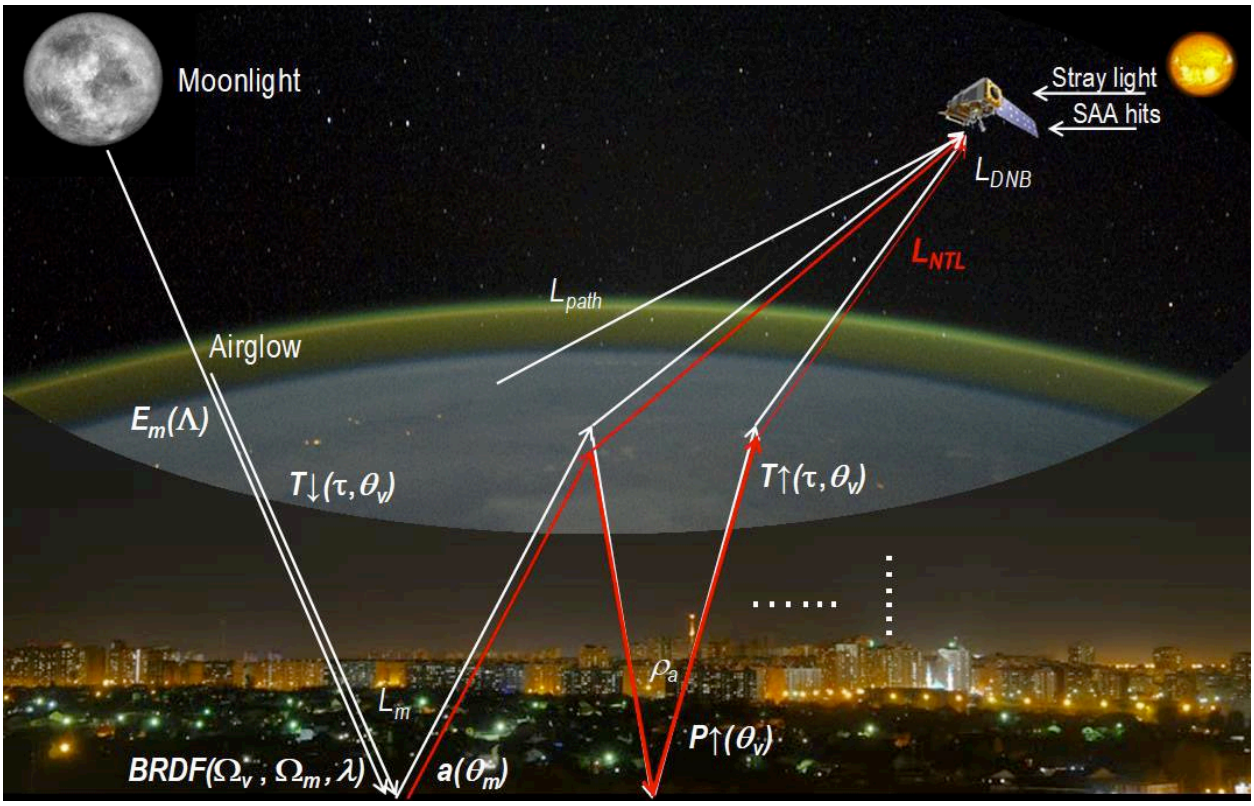

Figure 1 Overview of NASA's Black Marble retrieval strategy (*cf.*, Equation 1). During the ~50% portion of the lunar cycle when moonlight is present at the time of satellite observation, the surface upward radiance from artificial light emissions, L_{NTL} [units of nWatts·cm^{-2}·sr^{-1}], can be extracted from at-sensor nighttime radiance at TOA (L_{DNB}). L_{path} is the nighttime path radiance, $a(\theta_m)$ is the VIIRS-derived actual surface albedo. The atmospheric backscatter is given by ρ_a. $T_{\downarrow}(\tau,\theta_v)$ and $T_{\uparrow}(\tau,\theta_v)$ are the total transmittances along the lunar-ground and ground-sensor paths (respectively). $P_{\uparrow}(\theta_v)$ is the probability of the upward transmission of NTL emissions through the urban vegetation canopy.

2.3 BRDF Correction

The VNP46 algorithm estimates the actual moonlight, aerosol, and surface albedo contribution through analytical BRDF model inversion. This model has proven effective in removing biases introduced by extraneous sources of NTL emissions.

The surface BRDF, or reflectance anisotropy is governed by the angle and intensity of illumination – whether that illumination source is solar, lunar or from airglow – and by the structural complexity of the surface, resulting in variations in brightly illuminated regions and highly shadowed areas. The semi-empirical RossThick-LiSparse Reciprocal (RTLSR, or Ross-Li) BRDF model (Román et al., 2010; Roujean et al., 1992; Schaaf et al., 2002, Schaaf et al., 2011; Strahler et al., 1999) is advantageous in this regard, since (1) it is the most likely kernel-driven combination to capture the wide range of conditions affecting the VIIRS DNB on a global basis; (2) it allows robust analytical model inversion

with a pixel-specific estimate of uncertainty in the model parameters and linear combinations thereof (Lucht and Roujean, 2000); and (3) the scheme is flexible enough to allow us to easily adopt other kernels should they become available, and demonstrably superior for a particular scenario.

For VIIRS DNB acquisitions over snow-free and snow-covered surfaces, we define the spectral radiance contribution from moonlight, L_m,

$$\boldsymbol{L_m}(\Omega_v, \Omega_m, \boldsymbol{\Lambda}) = \frac{\boldsymbol{E_m}(\boldsymbol{\Lambda})}{\boldsymbol{\pi}} \boldsymbol{BRF}(\Omega_v, \Omega_m, \boldsymbol{\Lambda}) \cos(\boldsymbol{\theta_m}) \tag{2}$$

in terms of the Ross-Li model:

$$\boldsymbol{BRDF}(\Omega_v, \Omega_m, \boldsymbol{\Lambda}) \approx \frac{\boldsymbol{BRF}(\Omega_v, \Omega_m, \boldsymbol{\Lambda})}{\boldsymbol{\pi}} = \boldsymbol{f_{iso}}(\boldsymbol{\Lambda}) + \boldsymbol{f_{vol}}(\boldsymbol{\Lambda})\boldsymbol{K_{vol}}(\Omega_v, \Omega_m) + \boldsymbol{f_{geo}}(\boldsymbol{\Lambda})\boldsymbol{K_{geo}}(\Omega_v, \Omega_m) \tag{3}$$

Here, we define the wavelength for the narrowband instrument of interest as the weighted center, Λ, of the VIIRS DNB spectral band [0.5–0.9 µm]. Parameter $f_{iso}(\Lambda)$ is the isotropic scattering component and equal to the bidirectional reflectance for a pixel viewing zenith angle $\theta_v = 0$ and a lunar zenith angle $\theta_m = 0$. Parameter $f_{geo}(\Lambda)$ is the coefficient of the LiSparse-reciprocal geometric scattering kernel K_{geo}, derived for a sparse ensemble of surface casting shadows on a Lambertian background (Li and Strahler, 1992). Parameter $f_{vol}(\Lambda)$ is the coefficient for the RossThick volume scattering kernel K_{vol}, so called for its assumption of a dense leaf canopy (Ross, 2012).

To achieve a high-quality BRDF retrieval, the NASA Black Marble algorithm collects all available daytime, atmospherically corrected, VIIRS DNB bidirectional reflectance factor (BRF) over a multi-date period (normally 16 days) to establish the analytical solution for the Ross-Li BRDF model parameter values, $f_k(\Lambda)$. Note that during moon-free nights, when atmospheric airglow is the dominant emission source, the VNP46 algorithm sets the illumination geometry to near-nadir ($\theta_m = 10°$) and the lunar irradiance to $E_m(\Lambda) = 0.26\ \mathrm{nW \cdot m^{-2}}$ (Liao et al., 2013). This enables a BRDF correction even in the absence of moonlight.

2.3 Seasonal Vegetation Correction

Another known source of uncertainty in the retrieval of satellite-derived NTL is the influence of canopy-level foliage within the ground-to-sensor geometry path (Román and Stokes, 2015). This effect, which has been shown to reduce the magnitude of NTL at city-wide scales (Levin, 2017; Levin and Zhang, 2017), is most pronounced in temperate urban regions; where mixed and deciduous vegetation are most pervasive. Given its seasonal dependence, this occlusion effect (obscuration of surface light by foliage) should be proportional in magnitude to the density and vertical distribution pattern of leaves within a

given VIIRS DNB pixel. Hence, while the effect may be non-linear (due to the confluence of factors that control the seasonality, physiognomy, and vertical distribution of urban vegetation canopies), we can parameterize the effect using analytical models, which aim to retrieve canopy structure parameters from multi-angle remote sensing data (Chopping, 2006). With this concept in mind, we are employing a vegetation dispersion parameter, known as the clumping index, ψ, to parameterize the confined distribution of foliage within distinct canopy structures (Chen et al., 2005; Chen and Black, 1991; Jiao et al., 2018; Leblanc et al., 2005; Nilson, 1971):

$$\boldsymbol{P_{\uparrow}(\theta_v) = e^{-\psi G(\theta_v) LAI} / \cos(\theta_v)} \quad (4)$$

Here, $P_{\uparrow}(\theta_v)$ is the probability of the upward transmission of NTL emissions through the urban vegetation canopy (known as the gap fraction probability and hereafter termed the P_{gap} equation), $G(\theta_v)$ is the extinction coefficient that expresses the mean area projection of plant elements in the direction θ_v (being 0.5 for canopies with a random distribution of leaf angles), and *LAI* is the Leaf Area Index.

The P_{gap} equation can be inverted from available daily VIIRS BRDF-derived clumping index values, as done by Hill et al. (2011) and He et al. (2012). The VIIRS LAI retrievals are based on the current standard product (VNP15) (Park et al., 2017). In the case of poor-quality or missing LAI values (*e.g.*, when LAI is not retrieved over dense urban areas), we are employing the VIIRS LAI backup algorithm by using a look-up table (LUT) (Knyazikhin et al., 1999; Xiao et al., 2016) with normalized difference vegetation index (NDVI) generated from high-quality retrievals from the VIIRS NBAR product (Shuai et al., 2013).

3 Data Product Formats

The NASA's Black Marble product suite includes the daily at-sensor TOA nighttime radiance (VNP46A1), and the daily moonlight and atmosphere corrected NTL (VNP46A2) products at a 500 m geographic linear latitude/longitude (lat/lon) grid. The data are provided in the standard HDF5 – Hierarchical Data Format - Earth Observing System (HDF-EOS5) format[3].

3.1 Metadata

Metadata (data attributes) provide information about the time of data acquisition, input products, geographic location, output of the data product, satellite instrument, processing environment, and other

[3] For additional details: https://earthdata.nasa.gov/user-resources/standards-and-references/hdf-eos5

aspects of the product. More details of the VNP46A1 and VNP46A2 product metadata are listed in Appendix A and B.

3.2 Filenames

The filenames follow a naming convention, which gives useful information regarding the specific product. For example, the filename VNP46A1.A2015001.h08v05.001.2017012234657.h5 indicates:

(1) VNP46A1: Product Short Name;
(2) A2015001: Julian Date of Acquisition (A-YYYYDDD);
(3) h08v05: Tile Identifier (horizontalXXverticalYY);
(4) 001: Collection Version;
(5) 2017012234657: Julian Date of Production (YYYYDDDHHMMSS);
(6) h5: Data Format (HDF5).

3.3 Projection

The NASA's Black Marble product suite (VNP46) employs the standard VIIRS science algorithms and software that produce the DNB standard (radiance-based) products, and their corresponding ancillary layers in gridded (Level-2G, Level-3) linear lat/lon format (Figure 2). The gridding algorithms were modified to work with the VIIRS DNB-unique viewing geometry, which, unlike the VIIRS moderate and imagery bands, has a ground pixel footprint at a nearly constant size (742 m). The rationale behind the VIIRS DNB gridding approach is to select the nighttime observations from available 6-min swath granules (2366 km along track, ~3100 km across-track), that are the least affected by cloud cover and off-nadir viewing observations. The goal is to increase signal-to-noise, while maximizing coverage within a cell of the gridded projection (Tan et al., 2006; Wolfe et al., 2002). By implementing this combined gridding strategy and geographic linear lat/lon projection formats, we seek to improve the efficiency of processing and reprocessing the VNP46 product suite, preserve the satellite location and observation footprints, while also facilitating the products' handling by accessible, geographic information system (GIS)-friendly analysis and mapping software.

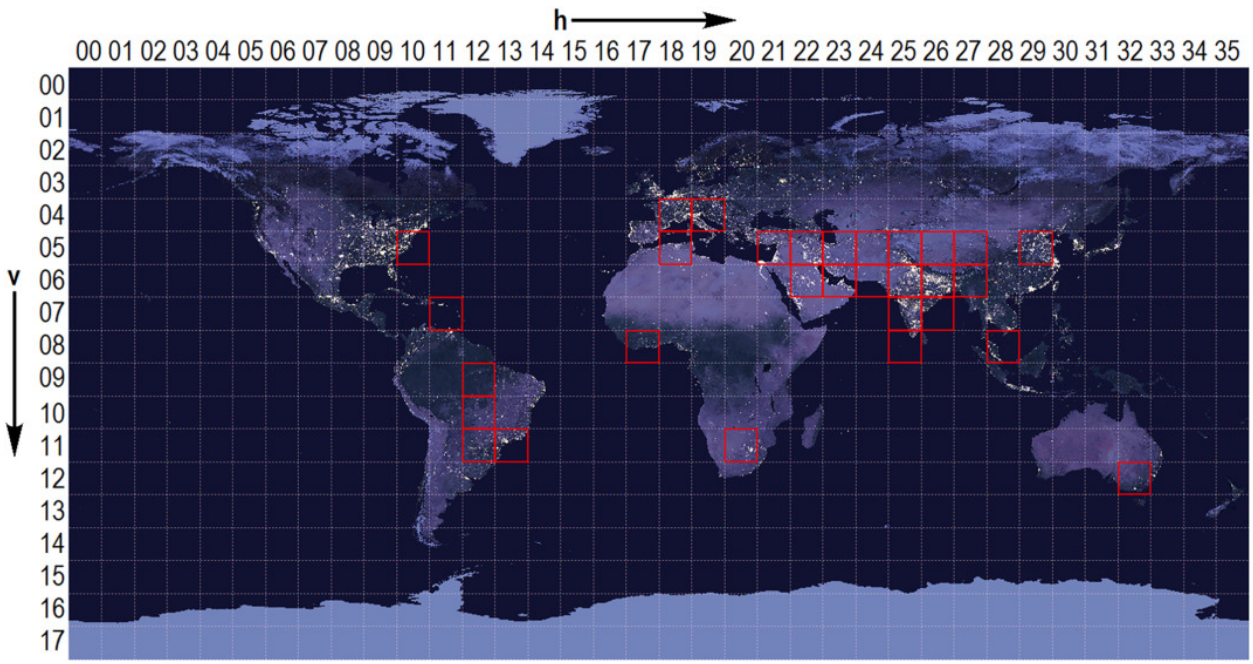

Figure 2 The Suomi-NPP VIIRS linear latitude/longitude (or geographic) grid consists of 460 non-overlapping Land tiles, which measure approximately 10°×10° region. Thirty VIIRS tiles (highlighted in red) were used to conduct the benchmark tests presented in NASA's Black Marble Nighttime Lights Product Suite ATBD.

4. Product generation

Data product inputs to the NASA Black Marble (VNP46) algorithm are listed in Table 1 and Table 2. The algorithm processing flow is depicted in Figure 3. The algorithm processing cycle is divided into daytime and nighttime branches, and each processing branch produces a unique set of ancillary and quality assurance (QA) flags.

Table 1 Black Marble VNP46A1 product input files

Input File	**Description**
VNP02DNB	VIIRS/NPP Day/Night Band 6-Min L1B Swath 750m (L1B DNB)
VNP02MOD	VIIRS/NPP Moderate Resolution 6-Min L1B Swath 750m (L1B moderate bands)
NPP DNBN*	VIIRS L2G DNB radiance
NPP DNBN angles*	VIIRS L2G DNB angles
NPP MOD*	VIIRS L2G moderate bands M10, M11, M12, M13, M15, M16
NPP PTDN*	VIIRS DNB pointer files
The standard VIIRS Cloud Mask (VCM)	VIIRS cloud mask

*Intermediate Products

Table 2 Black Marble VNP46A2 product input files

Input file	Description
VNP46A1	VIIRS/NPP Daily Gridded Day Night Band 500m Linear Lat Lon Grid Night
VNPLG43DNBA1	VIIRS/NPP DNB BRDF/Albedo Model Parameters Daily L3 Global 500m LLL Grid
VNPLG09GA	VIIRS/NPP Surface Reflectance Daily L2G Global 1km and 500m Linear Lat Lon Grid
VNP04LGA	VIIRS/NPP Aerosols Optical Thickness Daily L2G Global Linear Lat Lon Grid

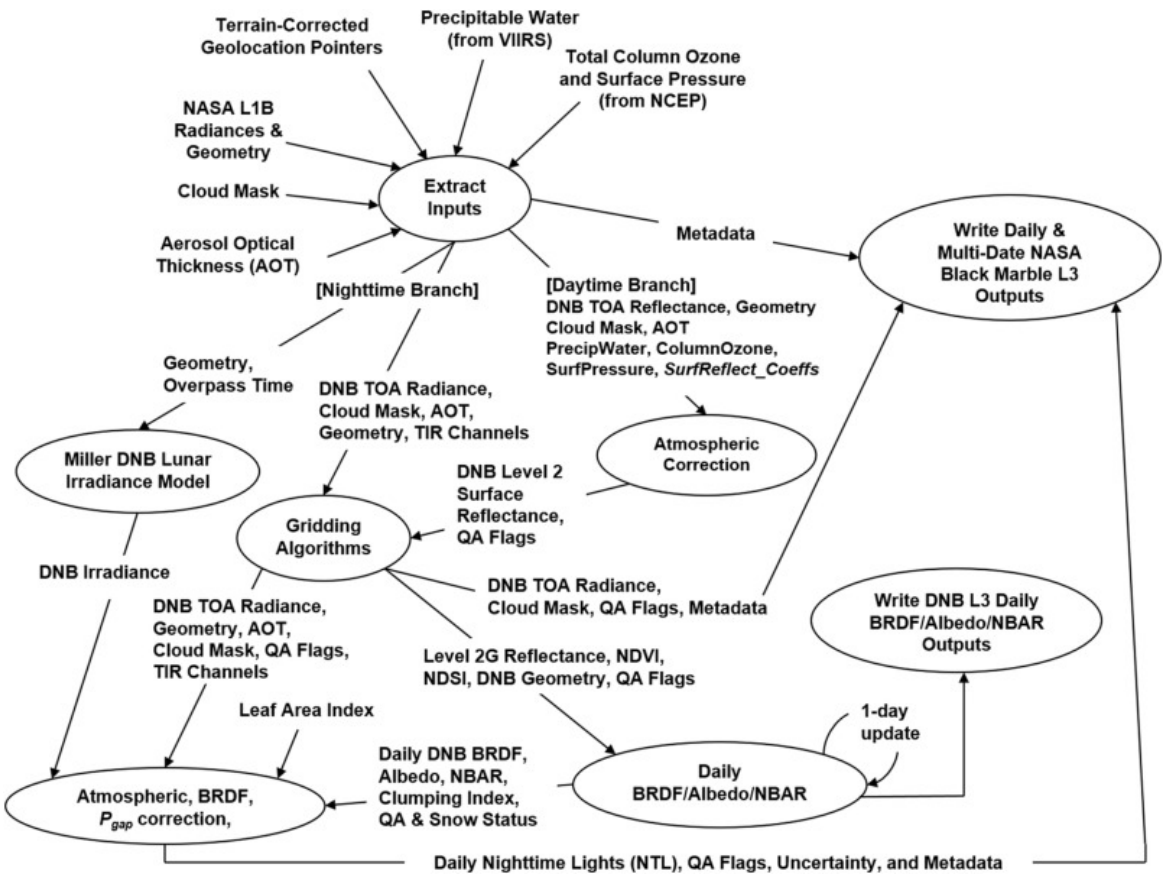

Figure 3 Algorithm processing cycle and ancillary parameters used by NASA's Black Marble product suite (VNP46).

For the daytime branch, science product generated executables (PGEs) based on the standard suite of VIIRS land products are integrated as part of NASA's Black Marble processing chain. First, a modified version of the operational VIIRS surface reflectance algorithm (Roger et al., 2016; Vermote et al., 2014) is used to generate the DNB surface bidirectional reflectance factor (BRF) using NASA's Level-1B calibrated radiance product as input (i.e., 6-minute granules, or 2366 km along-track and ~3100 km across-track). Level-2G DNB surface reflectance is then generated by performing spatial and temporal

aggregation to 500 m grid cells over daily time periods (Campagnolo et al., 2016; Pahlevan et al., 2017; Wolfe et al., 1998; Yang and Wolfe, 2001). Daily Level-3 DNB BRDF/Albedo data are then retrieved using the heritage MODIS/VIIRS algorithm (MCD43/VNP43) (Liu et al., 2017, Liu et al., 2017; Wang et al., 2018), and corresponding snow flags are estimated using the VIIRS Normalized Difference Snow Index (NDSI) algorithm (VNP10) (Riggs et al., 2016, Riggs et al., 2017). The NDVI and NDSI values are used to determine the growing, dormant, and snow periods to routinely update the *a priori* global database of the DNB BRDF product (Cescatti et al., 2012; Liu et al., 2017, Liu et al., 2017; Román et al., 2009). Surface BRF from the VIIRS I1 (red) and I2 (NIR) channels is used to obtain daily estimates of LAI (Knyazikhin et al., 1999; Park et al., 2017; Xiao et al., 2016). The retrieved LAI and clumping index values are then used to calculate the gap-fraction probability (Pgap).

The nighttime branch describes the path followed to generate the final VNP46 products. We begin with the at-sensor TOA nighttime radiance (VNP46A1), along with the corresponding nighttime cloud mask, multiple solar/viewing/lunar geometry values (including moon-illuminated fraction and phase angles), and the daily snow and aerosol status flags. These science data sets (SDS) enable open access to the primary inputs used to generate the NASA Black Marble NTL time-series record, thus ensuring reproducibility of the final outputs. A series of temporal and spatial gap-filling techniques are also employed to improve the coverage of the VNP46 NTL product.

5 Scientific Data Sets (SDS) from VNP46 Product Suite

5.1 The VNP46A1 Daily At-sensor TOA Nighttime Radiance Product

The daily at-sensor TOA nighttime radiance product (VNP46A1) is available at 500 m resolution from January 2012 onward. The 500m VNP46A1 product contains 26 SDS layers (Table 3) including sensor radiance, zenith and azimuth angles at-sensor, solar, and lunar, cloud mask flag, time, shortwave IR radiance, brightness temperatures, VIIRS quality flags, moon phase angle, and moon illumination fraction. Contents of VNP46A1 product are given in List 1. Table 3 presents detailed information on the layers. Table 4 and Table 5 present the details of the flag description keys and quality flags (QF) of the VNP46A1 product.

List 1 Datasets in a sample of VNP46A1 product.

- HDFEOS
  - ADDITIONAL
    - FILE_ATTRIBUTES
  - GRIDS
    - VNP_Grid_DNB
      - Data Fields
        - BrightnessTemperature_M12
        - BrightnessTemperature_M13
        - BrightnessTemperature_M15
        - BrightnessTemperature_M16
        - DNB_At_Sensor_Radiance_500m
        - Glint_Angle
        - Granule
        - Lunar_Azimuth
        - Lunar_Zenith
        - Moon_Illumination_Fraction
        - Moon_Phase_Angle
        - QF_Cloud_Mask
        - QF_DNB
        - QF_VIIRS_M10
        - QF_VIIRS_M11
        - QF_VIIRS_M12
        - QF_VIIRS_M13
        - QF_VIIRS_M15
        - QF_VIIRS_M16
        - Radiance_M10
        - Radiance_M11
        - Sensor_Azimuth
        - Sensor_Zenith
        - Solar_Azimuth
        - Solar_Zenith
        - UTC_Time
- HDFEOS INFORMATION
  - StructMetadata.0

Table 3 Scientific datasets included in the VNP46A1 daily at-sensor TOA nighttime radiance product

Scientific Datasets (SDS HDF Layers)	**Units**	**Description**	**Bit Type**	**Fill Value**	**Valid Range**	**Scale Factor**	**Offset**
DNB_At_Sensor_Radiance_500m	$nW \cdot cm^{-2} \cdot sr^{-1}$	At-sensor DNB radiance	16-bit unsigned integer	65535[4]	0 – 65534	0.1	0.0
Sensor_Zenith	Degrees	Sensor zenith angle	16-bit signed integer	-32768	-9000 – 9000	0.01	0.0
Sensor_Azimuth	Degrees	Sensor azimuth angle	16-bit signed integer	-32768	-18000 – 18000	0.01	0.0
Solar_Zenith	Degrees	Solar zenith angle	16-bit signed integer	-32768	0 – 18000	0.01	0.0
Solar_Azimuth	Degrees	Solar azimuth angle	16-bit signed integer	-32768	-18000 – 18000	0.01	0.0
Lunar_Zenith	Degrees	Lunar zenith angle	16-bit signed integer	-32768	0 – 18000	0.01	0.0
Lunar_Azimuth	Degrees	Lunar azimuth angle	16-bit signed integer	-32768	-18000 – 18000	0.01	0.0
Glint_Angle	Degrees	Moon glint angle	16-bit signed integer	-32768	-18000 – 18000	0.01	0.0
UTC_Time	Decimal hours	UTC time	32-bit floating point	-999.9	0 24	1.0	0.0
QF_Cloud_Mask[2]	Unitless	Cloud mask status	16-bit unsigned integer	65535	0 – 65534	N/A	N/A
QF_DNB[3]	Unitless	DNB quality flag	16-bit unsigned integer	65535	0 – 65534	N/A	N/A
Radiance_M10	$W \cdot m^{-2} \cdot \mu m^{-1} \cdot sr^{-1}$	Radiance in band M10	16-bit unsigned integer	65535	0 – 65534	0.0013	-0.04
Radiance_M11	$W \cdot m^{-2} \cdot \mu m^{-1} \cdot sr^{-1}$	Radiance in band M11	16-bit unsigned integer	65535	0 – 65534	0.00058	-0.02
BrightnessTemperature_M12	Kelvin	Brightness temperature of band M12	16-bit unsigned integer	65535	0 – 65534	0.0025	203.0

BrightnessTemperature_M13	Kelvin	Brightness temperature of band M13	16-bit unsigned integer	65535	0 – 65534	0.0025	203.0
BrightnessTemperature_M15	Kelvin	Brightness temperature of band M15	16-bit unsigned integer	65535	0 – 65534	0.0041	111.0
BrightnessTemperature_M16	Kelvin	Brightness temperature of band M16	16-bit unsigned integer	65535	0 – 65534	0.0043	103.0
QF_VIIRS_M10[4]	Unitless	Quality flag of band M10	16-bit unsigned integer	65535	0 – 65534	N/A	N/A
QF_VIIRS_M11[4]	Unitless	Quality flag of band M11	16-bit unsigned integer	65535	0 – 65534	N/A	N/A
QF_VIIRS_M12[4]	Unitless	Quality flag of band M12	16-bit unsigned integer	65535	0 – 65534	N/A	N/A
QF_VIIRS_M13[4]	Unitless	Quality flag of band M13	16-bit unsigned integer	65535	0 – 65534	N/A	N/A
QF_VIIRS_M15[4]	Unitless	Quality flag of band M15	16-bit unsigned integer	65535	0 – 65534	N/A	N/A
QF_VIIRS_M16[4]	Unitless	Quality flag of band M16	16-bit unsigned integer	65535	0 – 65534	N/A	N/A
Moon_Phase_Angle	Degrees	Moon phase angle	16-bit signed integer	-32768	0 – 18000	0.01	0.0
Moon_Illumination_Fraction	Percentage	Moon illumination fraction	16-bit signed integer	-32768	0 – 10000	0.01	0.0
Granule	Unitless	Number of selected Granule	8-bit unsigned integer	255	0 – 254	1.0	0.0

[1] Note that fill value can arise from various scenarios such as bad quality data, or if the solar zenith angle < 108 degrees since that is the nighttime cut-off used in the code.

[2] Details of QF_Cloud_Mask are shown in Table 4.

[3] The scale and offset are for nighttime. Users should check the quality flags and metadata for specific values.

[4] Details of QF_DNB and QF of VIIRS band M10/11/12/13/15/16 are shown in Table 5.

Table 4 Value of QF_Cloud_Mask in the VNP46A1 product

Bit	Flag description key	Interpretation
0	Day/Night	0 = Night 1 = Day
1-3	Land/Water Background	000 = Land & Desert 001 = Land no Desert 010 = Inland Water 011 = Sea Water 101 = Coastal
4-5	Cloud Mask Quality	00 = Poor 01 = Low 10 = Medium 11 = High
6-7	Cloud Detection Results & Confidence Indicator	00 = Confident Clear 01 = Probably Clear 10 = Probably Cloudy 11 = Confident Cloudy
8	Shadow Detected	1 = Yes 0 = No
9	Cirrus Detection (IR) (BTM15 – BTM16)	1 = Cloud 0 = No Cloud
10	Snow/ Ice Surface	1 = Snow/Ice 0 = No Snow/Ice

Table 5 Value of QF_DNB and QF of VIIRS band M10/11/12/13/15/16 in the VNP46A1 product

SDS Layer	Flag Mask Values and Descriptions
QF_DNB	1 = Substitute_Cal 2 = Out_of_Range 4 = Saturation 8 = Temp_not_Nominal 16 = Stray_light 256 = Bowtie_Deleted/Range_bit 512 = Missing_EV 1024 = Cal_Fail 2048 = Dead_Detector
QF_VIIRS_M10 QF_VIIRS_M11 QF_VIIRS_M12	1 = Substitute_Cal 2 = Out_of_Range 4 = Saturation

QF_VIIRS_M13 QF_VIIRS_M15 QF_VIIRS_M16	8 = Temp_not_Nominal 256 = Bowtie_Deleted 512 = Missing_EV 1024 = Cal_Fail 2048 = Dead_Detector

5.2 The VNP46A2 Daily Moonlight-adjusted Nighttime Lights (NTL) Product

The daily moonlight- and atmosphere-corrected NTL (VNP46A2) is available at 500 m resolution from January 2012-present. The VNP46A2 product has 6 layers containing information on BRDF-corrected NTL (500 m), lunar irradiance, mandatory quality flag, latest high-quality retrieval (number of days), snow flag, and cloud mask flag. Contents of VNP46A2 product are given in List 2. The detailed VNP46A2 layer properties are described in Table 6. Table 7 and Table 8 present the details of quality flags (QF) for the VNP46A2 product.

List 2 Datasets in a sample of VNP46A2 product

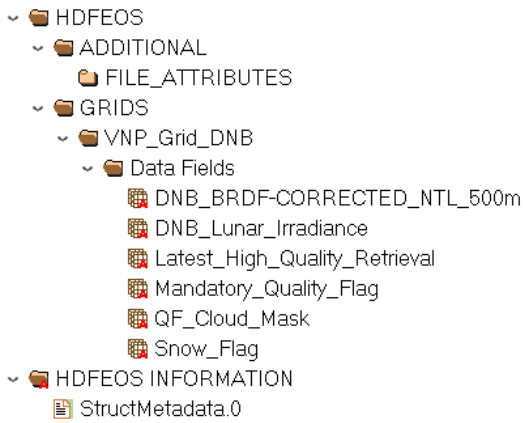

Table 6 Scientific datasets included in VNP46A2 daily moonlight-adjusted NTL product

Scientific Data Sets (SDS HDF Layers)	**Units**	**Description**	**Bit Types**	**Fill Value**	**Valid Range**	**Scale Factor**	**Offset**
DNB_BRDF-Corrected_NTL_500m	$nWatts \cdot cm^{-2} \cdot sr^{-1}$	BRDF-corrected DNB NTL	16-bit unsigned integer	65,535	0 – 65,534	0.1	0.0
DNB_Lunar_Irradiance	$nWatts \cdot cm^{-2}$	DNB Lunar Irradiance	16-bit unsigned integer	65,535	0 – 65,534	0.1	0.0
Mandatory_Quality_Flag[1]	Unitless	Mandatory quality flag	8-bit unsigned	255	0 – 3	N/A	N/A

			integer				
Latest_High_Quality_Retrieval	Number of days	Latest high quality BRDF corrected DNB radiance retrieval	8-bit unsigned integer	255	0 – 254	1.0	0.0
Snow_Flag[2]	Unitless	Flag for snow cover	8-bit unsigned integer	255	0 – 1	N/A	N/A
QF_Cloud_Mask[3]	Unitless	Quality flag for cloud mask	16-bit unsigned integer	65,535	0 – 65,534	N/A	N/A

[1] Details of Mandatory_Quality_Flag are shown in Table 7.

[2] Details of Snow_Flag are shown in Table 8.

[3] Details of QF_Cloud_Mask are shown in Table 4.

Table 7 Values of the Mandatory_Quality_Flag in VNP46A2 product

Value	Retrieval quality	Algorithm instance
00	High-quality	Main algorithm (Persistent nighttime lights)
01	High-quality	Main algorithm (Ephemeral Nighttime Lights)
02	Good-quality	Back-up algorithm (Temporal gap-filling)
03	Poor-quality	Main algorithm (Outlier, potential cloud contamination or other issues)
255	No retrieval	Fill value

Table 8 Values of the Snow_Flag in VNP46A2 product

Flag description key	Value	Interpretation
Snow/ Ice Surface	00	No Snow/Ice
	01	Snow/Ice
	255	Fill value

5.3 Examples of the VNP46 Product Suite

We plan to provide access to the VNP46 product suite both retrospectively, via NASA's Level-1 and Atmosphere Archive & Distribution System Distributed Active Archive Center (LAADS DAAC), and in forward near-real-time (NRT) data streams, via NASA's Land, Atmosphere Near-real-time Capability for EOS (LANCE) with a latency of about three hours. The NRT data are mainly used in response to

disasters and other management applications, which require quick turnaround time for both data processing and data access.

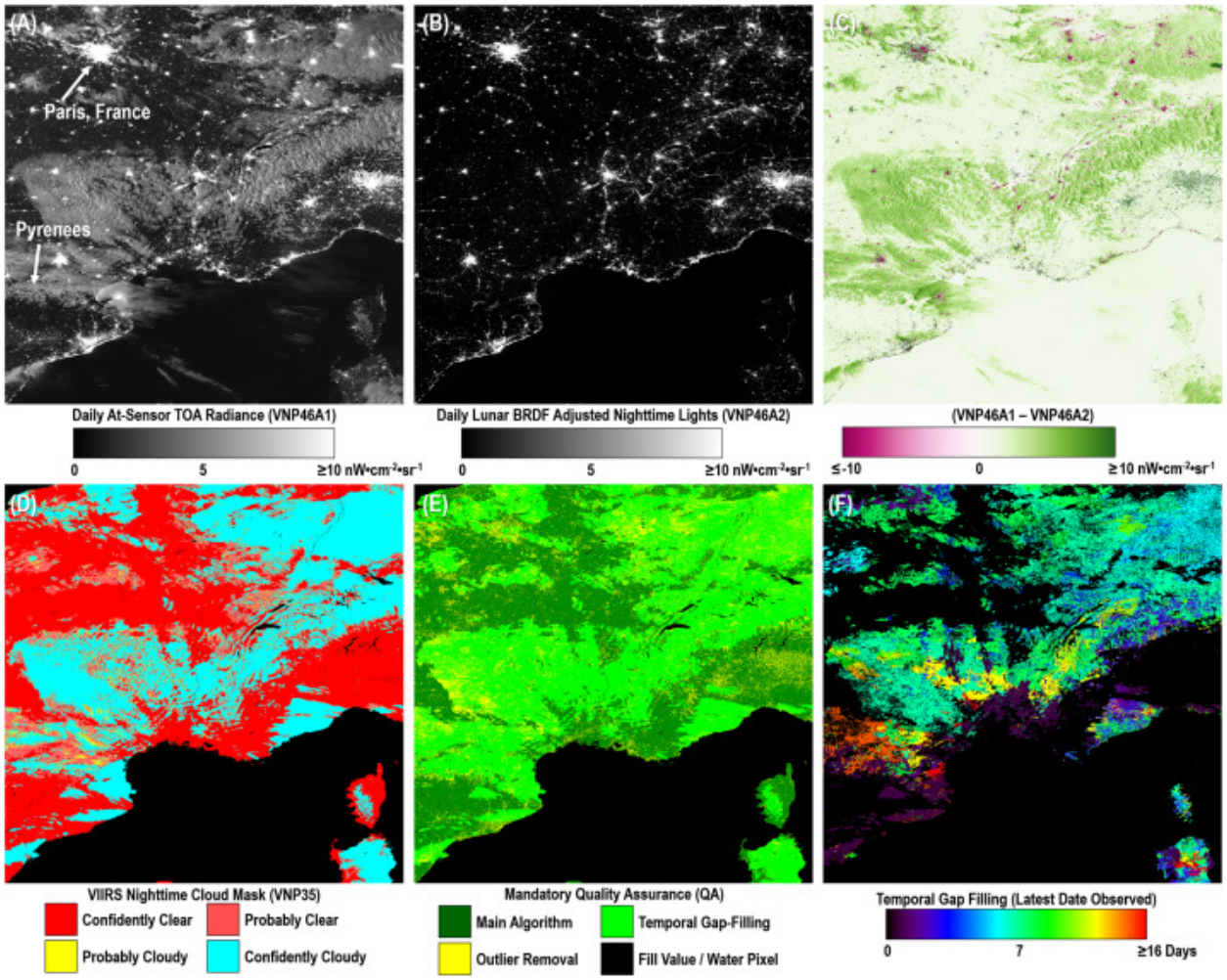

Figure 4 VNP46 product suite components for a 10° × 10° Level-3 tile over France and the Balearic Sea region (h18v04; DOY 2015-091). The full-moon-illuminated and 51% cloud-contaminated scene illustrates the challenges of nighttime cloud masking over snow-covered surfaces (e.g., the French Alps and the Pyrenees).

Figure 4 and Figure 5 illustrate the key processing steps used to retrieve high-quality NTL as part of NASA's Black Marble product suite. Cloud-free, atmospheric-, seasonal-, and moonlight BRDF-corrected DNB nighttime radiance is produced using the nighttime DNB-at-sensor radiance (VNP46A1), nighttime cloud mask, aerosol optical depth values, snow status flag, Ross-Li DNB BRDF model parameters and albedo values, Pgap, and per-pixel estimates of DNB lunar irradiance and corresponding geometries. A mandatory quality assurance (QA) flag is then provided to establish the pixel-specific estimates of retrieval performance. Note that when the temporal gap-filling routine is called upon, as reported in the mandatory quality assurance (QA) Flags (Table 7), the latest high-quality date observed (based on retrievals using the main algorithm) is reported as a separate SDS layer. If an outlier is still detected after

temporal gap-filling, then the VNP46 algorithm defaults to a monthly climatology, based on the most recently available moonless high QA values. Thus, through judicious use of the VNP46 product quality flag, the end-user can establish whether a particular temporally gap-filled NTL value is based on a recent date or not. This results in a traceable, moonlight-adjusted, NTL product to assess current versus recent NTL conditions, while reducing persistent data gaps caused by nighttime clouds, snow, and other ephemeral artifacts (e.g., the Aurora Borealis – cf., Figure 5).

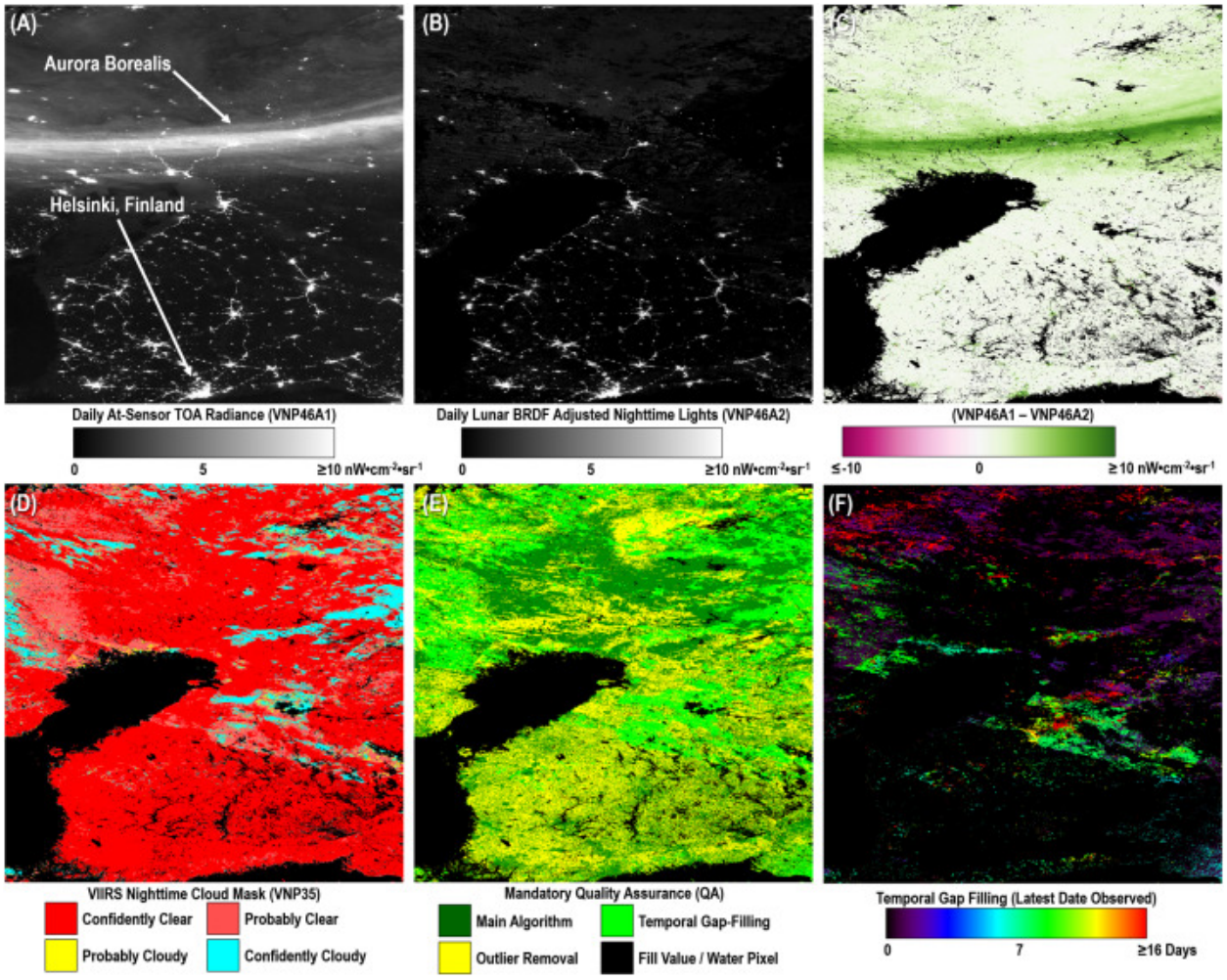

Figure 5 VNP46 product suite components for a 10° × 10° Level-3 tile over Sweden and Finland (h20v02; DOY 2013-080). The half-moon-illuminated and 30% cloud-contaminated scene is shown to capture extraneous light emissions north of the Gulf of Bothnia caused by the Aurora Borealis.

6 Evaluation and Validation of the Product

The overarching goal of NASA's Black Marble science product development effort is to achieve a "breakthrough" performance specification (cf.,Table 9) by conducting the following: (1) long-term stability monitoring of the entire VNP46 algorithm processing chain, including the fundamental (Level-

1B) VIIRS DNB time-series record, terrain-corrected geolocation, stray-light correction, and calibration LUTs; and (2) global quality assessment, uncertainty quantification, and product validation. To assess progress, we have developed a series of benchmark tests to quantify product performance at representative spatial and temporal scales. This comprehensive suite of benchmark tests and assessment metrics are meant to ensure that we can identify variations in VNP46 product performance quickly, and implement improvements in a timely fashion. It also enables the end-user to consider the products in their appropriate context, e.g., by anticipating appropriate noise reduction levels under specific retrieval conditions.

Table 9 Key performance metrics established for NASA's Black Marble product suite

Key performance metrics	**Threshold**	**Breakthrough**	**Goal**
NTL detection limit (Lmin)	3.0 $nW \cdot cm^{-2} \cdot sr^{-1}$	0.5 $nW \cdot cm^{-2} \cdot sr^{-1}$	0.25 $nW \cdot cm^{-2} \cdot sr^{-1}$
NTL robustness (L0)	±3.0 $nW \cdot cm^{-2} \cdot sr^{-1}$	± 0.10 $nW \cdot cm^{-2} \cdot sr^{-1}$	± 0.05 $nW \cdot cm^{-2} \cdot sr^{-1}$
Stray light error	0.45 $nW \cdot cm^{-2} \cdot sr^{-1}$	0.25 $nW \cdot cm^{-2} \cdot sr^{-1}$	< 0.1 $nW \cdot cm^{-2} \cdot sr^{-1}$
Spatial resolution	742m (±5%)	500m (±5%)	≤200m (±5%)
Temporal resolution	Monthly	Daily	Hourly
Geolocation uncertainty	133m	50m	20m

A series of benchmark tests were designed to quantify errors inherited from the upstream products (i.e., VIIRS calibrated radiance, cloud mask, aerosol retrieval, etc.), and provided a relative assessment of NTL product performance. The initial validation results are presented together with example case studies that are available in related publications in section 10. To establish the absolute accuracy of the final NTL retrievals, one must also assess the NTL products against an independent source of reference data. Unfortunately, quality-assessed in situ NTL measurements are not widely available; let alone, at the spatial and temporal densities necessary to capture the full range of retrieval conditions. Recent NASA Black Marble product validation efforts have therefore focused on developing guidelines for accuracy assessment of NTL products through a number of international initiatives.

Figure 6 shows an example of the accuracy assessment of NTL products through a field experiment at the Pitahaya farmland site in Cabo Rojo, PR. During the night of 2 March 2017, at 02:00 local time, the Puerto Rico's Working Group on Light Pollution (PRWGLP) team conducted a validation experiment at the Pitahaya site. A stable point source was reflected by a 30 m^2 Lambertian target to generate an in-band DNB radiance at sensor of ~0.45$nW \cdot cm^{-2} \cdot sr^{-1}$. Additional Sky-Quality Meter instrument data recordings (Falchi et al., 2016; Kyba et al., 2011, Kyba et al., 2013; Schnitt et al., 2013) with specialized filters matching the VIIRS relative spectral response, as well as atmospheric measurements from nearby

Aerosol Robotic Network (AERONET) sun photometers (Holben et al., 1998) were used to characterize atmospheric conditions.

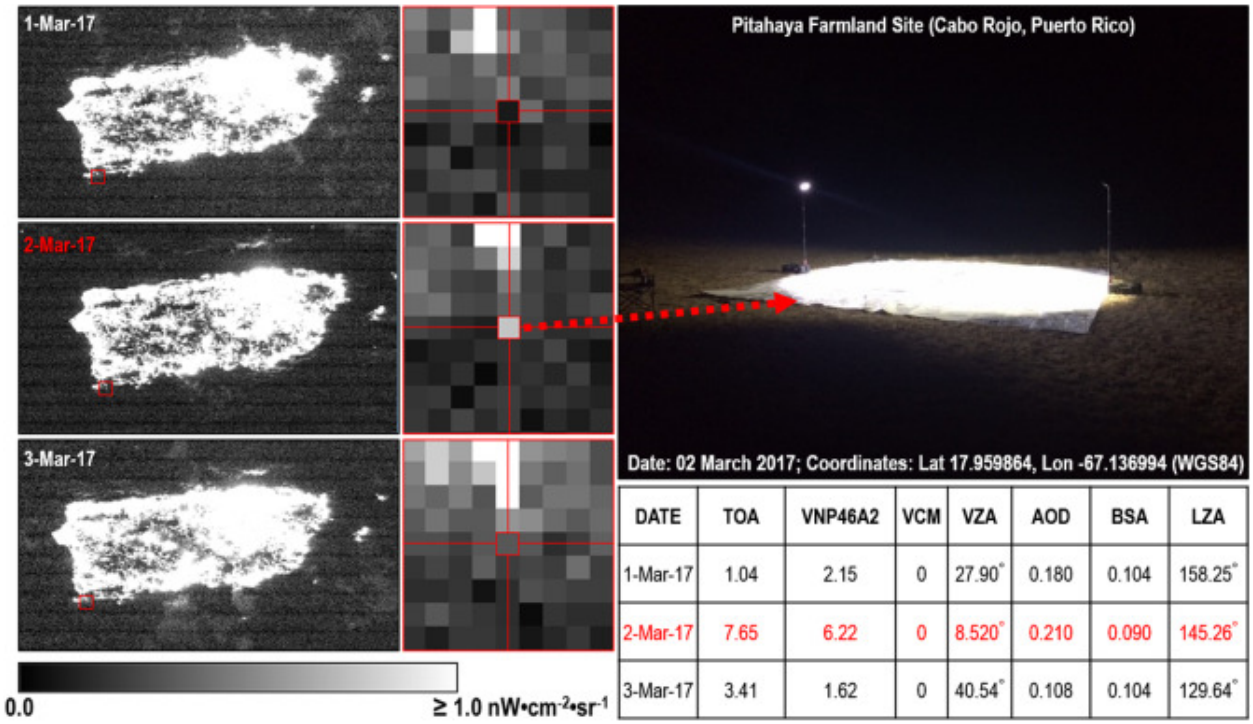

DATE	TOA	VNP46A2	VCM	VZA	AOD	BSA	LZA
1-Mar-17	1.04	2.15	0	27.90°	0.180	0.104	158.25°
2-Mar-17	7.65	6.22	0	8.520°	0.210	0.090	145.26°
3-Mar-17	3.41	1.62	0	40.54°	0.108	0.104	129.64°

Figure 6 The NTL radiance at the Pitahaya farmland site in Cabo Rojo, PR on 1st, 2nd and 3rd March 2017. The top-right image shows the setup of the stable point source. TOA and VNP46A2 values are in $nW \cdot cm^{-2} \cdot sr^{-1}$. VCM = 0 represents cloud free overpasses. LZA is lunar zenith angle, and the values larger than 108° correspond to moonless nights.

The validation approach follows the assessment method first described in Cao and Bai (2014), which relies on quantitative analysis and stability monitoring of stable light-point sources. We used the following parameters to generate our radiative transfer calculations: (1) atmospheric transmittance = 0.8 (based on 6S radiative transfer code and AERONET calculations), a target reflectance = 0.8, and 16 W of total effective irradiance incident on the reflective surface. Results in Figure 6 also illustrate how the detected VIIRS at-sensor cloud-corrected radiance (or TOA) and VNP46A2 estimates over the pixel centered on the reflective point source were within the VNP46A2 product's "breakthrough" requirement specifications for the NTL detection limit, Lmin (0.43 $nW \cdot cm^{-2} \cdot sr^{-1}$) after removing background noise measured the days prior and after activation of the stable light-point sources. We found that the final VNP46A2 product resulted in a 16.95% sensitivity enhancement (due to reduced background noise), as confirmed in previous benchmark tests, compared to the at-sensor cloud-corrected radiance product (TOA) under observed moon-free conditions.

7 Data Archives

The VNP46 suite of daily operational products are archived and supported by NASA's LAADS DAAC data center https://ladsweb.modaps.eosdis.nasa.gov/.

NASA's LANCE site will provide access to the VNP46 NRT suite with a latency of about three hours: https://earthdata.nasa.gov/earth-observation-data/near-real-time

8 Data Usage and Citation Policies

Please find detailed information on how to use and cite the data at the following site: https://lpdaac.usgs.gov/dataset_discovery/viirs/viirs_policies

9 Contact Information

Principal Investigator: Dr. Miguel O. Román (mroman@usra.edu)
Science Principal Investigator: Dr. Zhuosen Wang (zhuosen.wang@nasa.gov)
NASA Official: Dr. Virginia L. Kalb (virginia.l.kalb@nasa.gov)
NASA/GSFC, Mail Code: 619, Greenbelt, MD 20771

10 Related Publications

Román, M.O., Wang, Z., Sun, Q., Kalb, V., Miller, S.D., Molthan, A., Schultz, L., Bell, J., Stokes, E.C., Pandey, B. and Seto, K.C., et al. (2018). NASA's Black Marble nighttime lights product suite. Remote Sens. Environ. 210, 113-143. doi:10.1016/j.rse.2018.03.017.

Román, M.O. and Stokes, E.C. (2015). Holidays in lights: Tracking cultural patterns in demand for energy services. Earth's Future, 3, 182–205.

Wang, Z., Román, M. O., Sun, Q., Molthan, A. L., Schultz, L. A., and Kalb, V. L. (2018). Monitoring Disaster-related Power Outages Using NASA Black Marble Nighttime Light Product. Int. Arch. Photogramm. Remote Sens. Spatial Inf. Sci., XLII-3, 1853-1856, https://doi.org/10.5194/isprs-archives-XLII-3-1853-2018, 2018.

Wang, Z., Shrestha, R. and Román, M. O., (2018). NASA's Black Marble Nighttime Lights Product Suite Algorithm Theoretical Basis Document (ATBD), Version 1.0, April 2018. Available in https://viirsland.gsfc.nasa.gov/PDF/VIIRS_BlackMarble_ATBD_V1.0.pdf

Cole, T.A., Wanik, D.W., Molthan, A.L., Román, M.O. and Griffin, R.E. (2017). Synergistic use of nighttime satellite data, electric utility infrastructure, and ambient population to improve power outage detections in urban areas. Remote Sensing, 9 (3), 286. doi:10.3390/rs9030286.

References

Andersson, E., Barthel, S., Borgström, S., Colding, J., Elmqvist, T., Folke, C., Gren, Å., 2014. Reconnecting cities to the biosphere: stewardship of green infrastructure and urban ecosystem services. Ambio 43, 445–453.

Asanuma, I., Yamaguchi, T., Park, J., Mackin, K.J., Mittleman, J., 2016. Detection limit of fishing boats by the day night band (DNB) on VIIRS, in: SPIE Optical Engineering+ Applications. International Society for Optics and Photonics, p. 99760P–99760P–8.

Bankert, R.L., Solbrig, J.E., Lee, T.F., Miller, S.D., 2011. Automated lightning flash detection in nighttime visible satellite data. Weather Forecast. 26, 399–408.

Baret, F., NightingaleJ., Garrigues, S., Justice, C., Nickeson, J.E., 2009. Report on the CEOS Land Product Validation Sub-group Meeting. Earth Obs. 21, 26–30.

Bennett, M.M., Smith, L.C., 2017. Advances in using multitemporal night-time lights satellite imagery to detect, estimate, and monitor socioeconomic dynamics. Remote Sens. Environ. 192, 176–197. doi:10.1016/j.rse.2017.01.005

Bennie, J., Davies, T.W., Inger, R., Gaston, K.J., 2014. Mapping artificial lightscapes for ecological studies. Methods Ecol. Evol. 5, 534–540. doi:10.1111/2041-210X.12182

Bickenbach, F., Bode, E., Nunnenkamp, P., Söder, M., 2016. Night lights and regional GDP. Rev. World Econ. 152, 425–447. doi:10.1007/s10290-016-0246-0

Campagnolo, M.L., Sun, Q., Liu, Y., Schaaf, C., Wang, Z., Román, M.O., 2016. Estimating the effective spatial resolution of the operational BRDF, albedo, and nadir reflectance products from MODIS and VIIRS. Remote Sens. Environ. 175, 52–64.

Cao, C., Bai, Y., 2014. Quantitative Analysis of VIIRS DNB Nightlight Point Source for Light Power Estimation and Stability Monitoring. Remote Sens. 6, 11915–11935. doi:10.3390/rs61211915

Cao, C., Shao, X., Uprety, S., 2013. Detecting light outages after severe storms using the S-NPP/VIIRS day/night band radiances. IEEE Geosci. Remote Sens. Lett. 10, 1582–1586. doi:10.1109/LGRS.2013.2262258

Cescatti, A., Marcolla, B., Vannan, S.K.S., Pan, J.Y., Román, M.O., Yang, X., Ciais, P., Cook, R.B., Law, B.E., Matteucci, G., Migliavacca, M., Moors, E., Richardson, A.D., Seufert, G.G., Schaaf, C.B., 2012. Intercomparison of MODIS albedo retrievals and in situ measurements across the global FLUXNET network. Remote Sens. Environ. 121, 323–334. doi:10.1016/j.rse.2012.02.019

Chen, H., Xiong, X., Sun, C., Chen, X., Chiang, K., 2017. Suomi-NPP VIIRS day–night band on-orbit calibration and performance. J. Appl. Remote Sens. 11, 36019.

Chen, J.M., Black, T.A., 1991. Measuring leaf area index of plant canopies with branch architecture. Agric. For. Meteorol. 57, 1–12.

Chen, J.M., Menges, C.H., Leblanc, S.G., 2005. Global mapping of foliage clumping index using multi-angular satellite data. Remote Sens. Environ. 97, 447–457.

Chen, X., Nordhaus, W., 2015. A test of the new VIIRS lights data set: Population and economic output in Africa. Remote Sens. 7, 4937–4947. doi:10.3390/rs70404937

Chen, Z., Yu, B., Hu, Y., Huang, C., Shi, K., Wu, J., 2015. Estimating house vacancy rate in metropolitan areas using NPP-VIIRS nighttime light composite data. IEEE J. Sel. Top. Appl. Earth Obs. Remote Sens. 8, 2188–2197. doi:10.1109/JSTARS.2015.2418201

Chopping, M.J., 2006. Progress in retrieving canopy structure parameters from NASA multi-angle remote sensing, in: International, I. (Ed.), Proceedings of the IEEE International Geoscience & Remote Sensing Symposium, IGARSS '06 and the 27th Canadian Remote Sensing Symposium. Denver, CO, pp. 256–259.

Cinzano, P., Falchi, F., Elvidge, C.D., Baugh, K.E., 2000. The artificial night sky brightness mapped from DMSP satellite Operational Linescan System measurements. Mon. Not. R. Astron. Soc. 318, 641–657.

Cole, T.A., Wanik, D.W., Molthan, A.L., Román, M.O., Griffin, R.E., 2017. Synergistic Use of Nighttime Satellite Data, Electric Utility Infrastructure, and Ambient Population to Improve Power Outage Detections in Urban Areas. Remote Sens. 9, 286. doi:10.3390/rs9030286

Cook, B.D., Corp, L.A., Nelson, R.F., Middleton, E.M., Morton, D.C., McCorkel, J.T., Masek, J.G., Ranson, K.J., Ly, V., Montesano, P.M., 2013. NASA goddard's LiDAR, hyperspectral and thermal (G-LiHT) airborne imager. Remote Sens. 5, 4045–4066. doi:10.3390/rs5084045

Coscieme, L., Pulselli, F.M., Bastianoni, S., Elvidge, C.D., Anderson, S., Sutton, P.C., 2014. A thermodynamic geography: Night-time satellite imagery as a proxy measure of emergy. Ambio 43, 969–979. doi:10.1007/s13280-013-0468-5

Elvidge, C.D., Keith, D.M., Tuttle, B.T., Baugh, K.E., 2010. Spectral identification of lighting type and character. Sensors 10, 3961–3988.

Elvidge, C.D., Zhizhin, M., Baugh, K., Hsu, F.-C., 2015a. Automatic boat identification system for VIIRS low light imaging data. Remote Sens. 7, 3020–3036.

Elvidge, C.D., Zhizhin, M., Baugh, K., Hsu, F.-C., Ghosh, T., 2015b. Methods for global survey of natural gas flaring from visible infrared imaging radiometer suite data. Energies 9, 14.

Esch, T., Heldens, W., Hirne, A., Keil, M., Marconcini, M., Roth, A., Zeidler, J., Dech, S., Strano, E., 2017. Breaking new ground in mapping human settlements from space-The Global Urban Footprint. arXiv Prepr. arXiv1706.04862.

Esch, T., Marconcini, M., Felbier, A., Roth, A., Heldens, W., Huber, M., Schwinger, M., Taubenbock, H., Muller, A., Dech, S., 2013. Urban footprint processor-Fully automated processing chain generating settlement masks from global data of the TanDEM-X mission. IEEE Geosci. Remote Sens. Lett. 10, 1617–1621. doi:10.1109/LGRS.2013.2272953

Falchi, F., Cinzano, P., Duriscoe, D., Kyba, C.C.M., Elvidge, C.D., Baugh, K., Portnov, B.A., Rybnikova, N.A., Furgoni, R., 2016. The new world atlas of artificial night sky brightness. Sci. Adv. 2, e1600377.

Griggs, D., Stafford-smith, M., Gaffney, O., Rockström, J., Öhman, M.C., Steffen, W., Glaser, G., Kanie, N., Noble, I., 2015. Policy : Sustainable development goals for people and planet. Nature 495, 5–9. doi:10.1038/495305a

Guo, W., Lu, D., Wu, Y., Zhang, J., 2015. Mapping impervious surface distribution with integration of SNNP VIIRS-DNB and MODIS NDVI data. Remote Sens. 7, 12459–12477.

He, L., Chen, J.M., Pisek, J., Schaaf, C.B., Strahler, A.H., 2012. Global clumping index map derived from the MODIS BRDF product. Remote Sens. Environ. 119, 118–130.

Helios Global, 2017. Helios Global World Trends [WWW Document]. URL http://www.heliosglobalinc.com/world-trends-watch/ (accessed 10.24.17).

Heynen, N., Perkins, H.A., Roy, P., 2006. The political ecology of uneven urban green space: the impact of political economy on race and ethnicity in producing environmental inequality in Milwaukee. Urban Aff. Rev. 42, 3–25.

Hill, M.J., Román, M.O., Schaaf, C.B., 2011. Dynamics of vegetation indices in tropical and subtropical savannas defined by ecoregions and Moderate Resolution Imaging Spectroradiometer (MODIS) land cover. Geocarto Int. 1–39. doi:doi:10.1080/10106049.2011.626529

Hillger, D., Kopp, T., Lee, T., Lindsey, D., Seaman, C., Miller, S., Solbrig, J., Kidder, S., Bachmeier, S., Jasmin, T., 2013. First-light imagery from Suomi NPP VIIRS. Bull. Am. Meteorol. Soc. 94, 1019–1029.

Holben, B.N., Eck, T.F., Slutsker, I., Tanré, D., Buis, J.P., Setzer, A., Vermote, E., Reagan, J.A., Kaufman, Y.J., Nakajima, T., Lavenu, F., Jankowiak, I., Smirnov, A., 1998. AERONET–A federated instrument network and data archive for aerosol characterization. Remote Sens. Environ. 66, 1–16. doi:doi:10.1016/S0034-4257(98)00031-5

Hu, C., Chen, S., Wang, M., Murch, B., Taylor, J., 2015. Detecting surface oil slicks using VIIRS nighttime imagery under moon glint: a case study in the Gulf of Mexico. Remote Sens. Lett. 6, 295–301.

Huang, Q., Yang, X., Gao, B., Yang, Y., Zhao, Y., 2014. Application of DMSP/OLS nighttime light images: A meta-analysis and a systematic literature review. Remote Sens. 6, 6844–6866. doi:10.3390/rs6086844

Jim, C.Y., 2004. Green-space preservation and allocation for sustainable greening of compact cities. Cities 21, 311–320.

Johnson, R.S., Zhang, J., Hyer, E.J., Miller, S.D., Reid, J.S., 2013. Preliminary investigations toward nighttime aerosol optical depth retrievals from the VIIRS day/night band. Atmos. Meas. Tech. 6, 587–612.

Kabisch, N., Haase, D., 2014. Green justice or just green? Provision of urban green spaces in Berlin, Germany. Landsc. Urban Plan. 122, 129–139.

Katz, Y., Levin, N., 2016. Quantifying urban light pollution - A comparison between field measurements and EROS-B imagery. Remote Sens. Environ. 177, 65–77. doi:10.1016/j.rse.2016.02.017

Klein, A.G., Stroeve, J., 2002. Development and validation of a snow albedo algorithm for the MODIS instrument. Ann. Glaciol. 34, 45–52.

Knyazikhin, Y., Glassy, J., Privette, J.L., Tian, Y., Lotsch, A., Zhang, Y., Wang, Y., Morisette, J.T., P.Votava, Myneni, R.B., Nemani, R.R., Running, S.W., 1999. MODIS Leaf Area Index (LAI) and Fraction of Photosynthetically Active Radiation Absorbed by Vegetation (FPAR) Product (MOD15) Algorithm Theoretical Basis Document, http://eospso.gsfc.nasa.gov/atbd/modistables.html.

Kopp, T.J., Thomas, W., Heidinger, A.K., Botambekov, D., Frey, R.A., Hutchison, K.D., Iisager, B.D., Brueske, K., Reed, B., 2014. The VIIRS Cloud Mask: Progress in the first year of S‐NPP toward a common cloud detection scheme. J. Geophys. Res. Atmos. 119, 2441–2456.

Kyba, C.C.M., Ruhtz, T., Fischer, J., Hölker, F., 2011. Cloud coverage acts as an amplifier for ecological light pollution in urban ecosystems. PLoS One 6, e17307.

Kyba, C.C.M., Wagner, J.M., Kuechly, H.U., Walker, C.E., Elvidge, C.D., Falchi, F., Ruhtz, T., Fischer, J., Hölker, F., 2013. Citizen Science Provides Valuable Data for Monitoring Global Night Sky Luminance. Sci. Rep. 3, 1835. doi:10.1038/srep01835

Lacaze, R., Chen, J.M., Roujean, J.-L., Leblanc, S.G., 2002. Retrieval of vegetation clumping index using hot spot signatures measured by POLDER instrument. Remote Sens. Environ. 79, 84–95. doi:doi:10.1016/S0034-4257(01)00241-3

Leblanc, S.G., Chen, J.M., White, H.P., Latifovic, R., Lacaze, R., Roujean, J.-L., 2005. Canada-wide foliage clumping index mapping from multiangular POLDER measurements. Can. J. Remote Sens. 31, 364–376.

Lee, S., Chiang, K., Xiong, X., Sun, C., Anderson, S., 2014. The S-NPP VIIRS Day-Night Band on-orbit calibration/characterization and current state of SDR products. Remote Sens. 6, 12427–12446.

Lee, S., McIntire, J., Oudrari, H., Schwarting, T., Xiong, X., 2015. A New Method for Suomi-NPP VIIRS Day–Night Band On-Orbit Radiometric Calibration. IEEE Trans. Geosci. Remote Sens. 53, 324–334. doi:10.1109/TGRS.2014.2321835

Levin, N., 2017. The impact of seasonal changes on observed nighttime brightness from 2014 to 2015 monthly VIIRS DNB composites. Remote Sens. Environ. 193, 150–164. doi:10.1016/j.rse.2017.03.003

Levin, N., Zhang, Q., 2017. A global analysis of factors controlling VIIRS nighttime light levels from densely populated areas. Remote Sens. Environ. 190, 366–382. doi:10.1016/j.rse.2017.01.006

Li, X., Xu, H., Chen, X., Li, C., 2013. Potential of NPP-VIIRS nighttime light imagery for modeling the regional economy of China. Remote Sens. 5, 3057–3081. doi:10.3390/rs5063057

Liao, L.B., Weiss, S., Mills, S., Hauss, B., 2013. Suomi NPP VIIRS day-night band on-orbit performance. J. Geophys. Res. Atmos. 118, 12705–12718. doi:10.1002/2013JD020475

Liu, Y., Wang, Z., Sun, Q., Erb, A.M., Li, Z., Schaaf, C.B., Zhang, X., Román, M.O., Scott, R.L., Zhang, Q., 2017. Evaluation of the VIIRS BRDF, Albedo and NBAR products suite and an assessment of continuity with the long term MODIS record. Remote Sens. Environ. 201, 256–274.

Liu, Hu, C., Zhan, W., Sun, C., Murch, B., Ma., L., 2017. Identifying industrial heat sources using time-series of the VIIRS Nightfire product with an object-oriented approach. Remote Sens. Environ. doi:10.1016/J.RSE.2017.10.019

Lucht, W., Roujean, J., 2000. Considerations in the parametric modeling of BRDF and albedo from multiangular satellite sensor observations. Remote Sens. Rev. 18, 343–379.

Ma, T., Zhou, C.H., Pei, T., Haynie, S., Fan, J.F., 2014. Responses of Suomi- NPP VIIRS- derived nighttime lights to socioeconomic activity in China's cities. Remote Sens. Lett. 5, 165–174. doi:10.1080/2150704x.2014.890758

Mann, M.L., Melaas, E.K., Malik, A., 2016. Using VIIRS Day/Night Band to Measure Electricity Supply Reliability: Preliminary Results from Maharashtra, India. Remote Sens. 8, 711.

McHardy, T.M., Zhang, J., Reid, J.S., Miller, S.D., Hyer, E.J., Kuehn, R.E., 2015. An improved method for retrieving nighttime aerosol optical thickness from the VIIRS Day/Night Band. Atmos. Meas. Tech. 8, 4773–4783.

Miller, S.D., Combs, C.L., Kidder, S.Q., Lee, T.F., 2012. Assessing Moonlight Availability for Nighttime Environmental Applications by Low-Light Visible Polar-Orbiting Satellite Sensors. J. Atmos. Ocean. Technol. 29, 538–557. doi:10.1175/JTECH-D-11-00192.1

Miller, S.D., Haddock, S.H.D., Elvidge, C.D., Lee, T.F., 2006. Twenty thousand leagues over the seas: the first satellite perspective on bioluminescent "milky seas." Int. J. Remote Sens. 27, 5131–5143. doi:10.1080/01431160600554298

Miller, S.D., Haddock, S.H.D., Elvidge, C.D., Lee, T.F., 2005. Detection of a bioluminescent milky sea from space. PNAS 102, 14181–14184. doi:doi:10.1073/pnas.0507253102

Miller, S.D., Straka, W., Mills, S.P., Elvidge, C.D., Lee, T.F., Solbrig, J., Walther, A., Heidinger, A.K., Weiss, S.C., 2013. Illuminating the capabilities of the suomi national polar-orbiting partnership (NPP) visible infrared imaging radiometer suite (VIIRS) day/night band. Remote Sens. 5, 6717–6766.

Miller, S.D., Straka, W.C., Yue, J., Smith, S.M., Alexander, M.J., Hoffmann, L., Setvák, M., Partain, P.T., 2015. Upper atmospheric gravity wave details revealed in nightglow satellite imagery. Proc. Natl. Acad. Sci. 112, E6728–E6735.

Miller, S.D., Turner, R.E., 2009. A Dynamic Lunar Spectral Irradiance Data Set for NPOESS/VIIRS Day/Night Band Nighttime Environmental Applications. IEEE Trans. Geosci. Remote Sens. 47, 2316–2329.doi:10.1109/TGRS.2009.2012696

Miller, Mills, S.P., Elvidge, C.D., Lindsey, D.T., Lee, T.F., Hawkins, J.D., 2012. Suomi satellite brings to light a unique frontier of nighttime environmental sensing capabilities. Proc. Natl. Acad. Sci. 109, 15706–15711. doi:doi:10.1073/pnas.1207034109

Mills, S., Miller, S., 2016. VIIRS Day/Night Band—Correcting Striping and Nonuniformity over a Very Large Dynamic Range. J. Imaging 2, 9. doi:doi:10.3390/jimaging2010009

Mills, S., Weiss, S., Liang, C., 2013. VIIRS day/night band (DNB) stray light characterization and correction, in: SPIE Optical Engineering+ Applications. International Society for Optics and Photonics, p. 88661P–88661P.

Minnis, P., Hong, G., Sun-Mack, S., Smith, W.L., Chen, Y., Miller, S.D., 2016. Estimating nocturnal opaque ice cloud optical depth from MODIS multispectral infrared radiances using a neural network method. J. Geophys. Res. Atmos. 121, 4907–4932. doi:10.1002/2015JD024456

Molthan, A., Jedlovec, G., 2013. Satellite observations monitor outages from Superstorm Sandy. Eos, Trans. Am. Geophys. Union 94, 53–54.

Moody, E.G., King, M.D., Schaaf, C.B., Platnick, S., 2008. MODIS-derived spatially complete surface albedo products: Spatial and temporal pixel distribution and zonal averages. J. Appl. Meteorol. Climatol. 47, 2879–2894. doi:doi:10.1175/2008JAMC1795.1

Moorthi, S., Pan, H.-L., Caplan, P., 2001. Changes to the 2001 NCEP operational MRF/AVN global analysis/forecast system. US Department of Commerce, National Oceanic and Atmospheric Administration, National Weather Service, Office of Meteorology, Program and Plans Division.

Morisette, J.T., Baret, F., Liang, S., 2006. Special issue on global land product validation. IEEE Trans. Geosci. Remote Sens. 44, 1695–1697.

Moustafa, S.E., Rennermalm, A.K., Román, M.O., Wang, Z., Schaaf, C.B., Smith, L.C., Koenig, L.S., Erb, A., 2017. Evaluation of satellite remote sensing albedo retrievals over the ablation area of the southwestern Greenland ice sheet. Remote Sens. Environ. 198, 115–125.

NASM, 2018. Thriving on Our Changing Planet: A Decadal Strategy for Earth Observation from Space. The National Academies Press, Washington, DC. doi:10.17226/24938

Nicodemus, F.E., 1977. Geometrical considerations and nomenclature for reflectance, in: National Bureau of Standards Monograph, No. 160. Washington, DC, pp. 1–52.Nilson, T., 1971. A theoretical analysis of the frequency of gaps in plant stands. Agric. Meteorol. 8, 25–38.

NRC, 2017. A look into Zaatari camp during winter | NRC [WWW Document]. World Bank. URL https://www.nrc.no/news/2016/february/a-look-into-zaatari-camp-during-winter/ (accessed 10.24.17).

O'Sullivan, F., 2017. How Built-Out Barcelona Found Space for an Urban Forest - CityLab [WWW Document]. URL https://www.citylab.com/solutions/2017/05/barcelona-green-urban-forest-climate-plan/526998/ (accessed 6.28.17).

Oda, T., Lauvaux, T., Lu, D., Rao, P., Miles, N.L., Richardson, S.J., Gurney, K.R., 2017. On the impact of granularity of space-based urban CO 2 emissions in urban atmospheric inversions: A case study for Indianapolis, IN. Elem Sci Anth 5.

Omar, A.H., Winker, D.M., Tackett, J.L., Giles, D.M., Kar, J., Liu, Z., Vaughan, M.A., Powell, K.A., Trepte, C.R., 2013. CALIOP and AERONET aerosol optical depth comparisons: One size fits none. J. Geophys. Res. Atmos. 118, 4748–4766.

Ou, J., Liu, X., Li, X., Li, M., Li, W., 2015. Evaluation of NPP-VIIRS nighttime light data for mapping global fossil fuel combustion CO 2 emissions: a comparison with DMSP-OLS nighttime light data. PLoS One 10, e0138310. doi:10.1371/journal.pone.0138310

Pahlevan, N., Sarkar, S., Devadiga, S., Wolfe, R.E., Román, M., Vermote, E., Lin, G., Xiong, X., 2017. Impact of Spatial Sampling on Continuity of MODIS–VIIRS Land Surface Reflectance Products: A Simulation Approach. IEEE Trans. Geosci. Remote Sens. 55, 183–196.

Park, T., Yan, K., Chen, C., Xu, B., Knyazikhin, Y., Myneni, R., 2017. VIIRS Leaf Area Index (LAI) and Fraction of Photosynthetically Active Radiation Absorbed by Vegetation (FPAR) Product Algorithm Theoretical Basis Document (ATBD), NASA Technical Report.

Paynter, I., Saenz, E., Genest, D., Peri, F., Erb, A., Li, Z., Wiggin, K., Muir, J., Raumonen, P., Schaaf, E.S., 2016. Observing ecosystems with lightweight, rapid‐scanning terrestrial lidar scanners. Remote Sens. Ecol. Conserv. 2, 174–189.

Polivka, T.N., Wang, J., Ellison, L.T., Hyer, E.J., Ichoku, C.M., 2016. Improving Nocturnal Fire Detection With the VIIRS Day–Night Band. IEEE Trans. Geosci. Remote Sens. 54, 5503–5519.

Riggs, G.A., Hall, D.K., Román, M.O., 2017. Overview of NASA's MODIS and VIIRS Snow-Cover Earth System Data Records. Earth Syst. Sci. Data 9, 1–13. doi:10.5194/essd-9-765-2017

Riggs, G.A., Hall, D.K., Román, M.O., 2016. NASA S-NPP VIIRS Snow Products Collection 1 User Guide 1–26. doi:doi:10.5067/VIIRS/VNP10_L2.v001

Roger, J.C., Vermote, E.F., Devadiga, S., Ray, J.P., 2016. Suomi-NPP VIIRS Surface Reflectance User's Guide.

Román, M., Schaaf, C.B., Yang, X., Woodcock, C.E., Strahler, A.H., Braswell, R.H., Curtis, P.S., Davis, K.J., D., D., Gu, L., Goulden, M.L., Hollinger, D.Y., Kolb, T.E., Meyers, T.P., Munger, J.W., Privette, J.L., Richardson, A.D., Wilson, T.B., Wofsy, S.C., 2009. The MODIS (Collection V005) BRDF/albedo product: Assessment of spatial representativeness over forested landscapes. Remote Sens. Environ. 113, 2476–2498. doi:doi:10.1016/j.rse.2009.07.009

Román, M.O., Gatebe, C.K., Poudyal, R., Schaaf, C.B., Wang, Z., King, M.D., 2011. Variability in surface BRDF at different spatial scales (30 m-500 m) over a mixed agricultural landscape as retrieved from airborne and satellite spectral measurements. Remote Sens. Environ. 115, 2184–2203. doi:10.1016/j.rse.2011.04.012

Román, M.O., Gatebe, C.K., Shuai, Y., Wang, Z., Gao, F., Masek, J.G., He, T., Liang, S., Schaaf, C.B., 2013. Use of In Situ and Airborne Multiangle Data to Assess MODIS- and Landsat-Based Estimates of Directional Reflectance and Albedo. IEEE Trans. Geosci. Remote Sens. 51, 1393–1404. doi:10.1109/TGRS.2013.2243457

Román, M.O., Schaaf, C.B., Lewis, P., Gao, F., Anderson, G.P., Privette, J.L., Strahler, A.H., Woodcock, C.E., Barnsley, M., 2010. Assessing the coupling between surface albedo derived from MODIS and the fraction of diffuse skylight over spatially-characterized landscapes. Remote Sens. Environ. 114, 738–760. doi:10.1016/j.rse.2009.11.014

Román, M.O., Stokes, E.C., 2015. Holidays in lights: Tracking cultural patterns in demand for energy services. Earth's Futur. 3, 182–205. doi:10.1002/2014EF000285

Román, M.O., Wang, Z., Sun, Q., Kalb, V., Miller, S.D., Molthan, A., Schultz, L., Bell, J., Stokes, E.C., Pandey, B. and Seto, K.C., et al. (2018). NASA's Black Marble nighttime lights product suite. Remote Sens. Environ., 210, 113-143. doi:10.1016/j.rse.2018.03.017.

Roujean, J., Leroy, M., Deschanms, P., 1992. A bidirectional reflectance model of the Earth's surface for the correction of remote sensing data. J. Geophys. Res. 97, 20,420-455,468. doi:doi:10.1029/92JD01411

Schaaf, C.B., Gao, F., Strahler, A.H., Lucht, W., Li, X., Tsang, T., Strugnell, N.C., Zhang, X., Jin, Y., Muller, J.P.J.-P., Lewis, P., Barnsley, M., Hobson, P., Disney, M., Roberts, G., Dunderdale, M., Doll, C., d'Entremont, R.P., Hu, B., Liang, S., Privette, J.L., Roy, D.P., 2002. First operational BRDF, albedo nadir reflectance products from MODIS. Remote Sens. Environ. 83, 135–148. doi:10.1016/S0034-4257(02)00091-3

Schaaf, Liu, J., Gao, F., Strahler, A.H., 2011a. MODIS albedo and reflectance anisotropy products from Aqua and Terra, in: Ramachandran, B., Justice, C., Abrams, M. (Eds.), Land Remote Sensing and Global Environmental Change: NASA's Earth Observing System and the Science of ASTER and MODIS. Springer-Verlag. ISBN:1441967486., p. 873.

Schaaf, Wang, Z., Strahler, A., 2011b. Commentary on Wang and Zender—MODIS snow albedo bias at high solar zenith angles relative to theory and to in situ observations in Greenland. Remote Sens. Environ. 115, 1296–1300.

Schaepman-Strub, G., Schaepman, M.E., Painter, T.H., Dangel, S., Martonchik, J. V, 2006. Reflectance quantities in optical remote sensing-definitions and case studies. Remote Sens. Environ. 103, 27–42. doi:doi:10.1016/j.rse.2006.03.002

Schnitt, S., Ruhtz, T., Fischer, J., Hölker, F., Kyba, C., 2013. Temperature stability of the sky quality meter. Sensors 13, 12166–12174.

Seto, K.C., Dhakal, S., 2014. Chapter 12: Human Settlements, Infrastructure, and Spatial Planning. Clim. Chang. 2014 Mitig. Clim. Chang. Contrib. Work. Gr. III to Fifth Assess. Rep. Intergov. Panel Clim. Chang. 67–76.

Sharma, R.C., Tateishi, R., Hara, K., Gharechelou, S., Iizuka, K., 2016. Global mapping of urban built-up areas of year 2014 by combining MODIS multispectral data with VIIRS nighttime light data. Int. J. Digit. Earth 9, 1004–1020. doi:10.1080/17538947.2016.1168879

Shi, K., Huang, C., Yu, B., Yin, B., Huang, Y., Wu, J., Chang, H., Bailang, Y., Bing, Y., Yixiu, H., Jianping, W., 2014. Evaluation of NPP-VIIRS night-time light composite data for extracting built-up urban areas. Remote Sens. Lett. 5, 358–366. doi:10.1080/2150704x.2014.905728

Shuai, Y., Schaaf, C., Zhang, X., Strahler, A., Roy, D., Morisette, J., Wang, Z., Nightingale, J., Nickeson, J., Richardson, A.D., 2013. Daily MODIS 500 m reflectance anisotropy direct broadcast (DB) products for monitoring vegetation phenology dynamics. Int. J. Remote Sens. 34, 5997–6016.

Skakun, S., Justice, C.O., Vermote, E., Roger, J.-C., 2018. Transitioning from MODIS to VIIRS: an analysis of inter-consistency of NDVI data sets for agricultural monitoring. Int. J. Remote Sens. 39, 971–992.

Strahler, A.H., Lucht, W., Schaaf, C.B., Tsang, T., Gao, F., Li, X., Muller, J.-P., Lewis, P., Barnsley, M., 1999. MODIS BRDF/Albedo Product: Algorithm Theoretical Basis Document Version 5.0. Technical Report. NASA EOS-MODIS.

Straka, W.C., Seaman, C.J., Baugh, K., Cole, K., Stevens, E., Miller, S.D., 2015. Utilization of the suomi national polar-orbiting partnership (npp) visible infrared imaging radiometer suite (viirs) day/night band for arctic ship tracking and fisheries management. Remote Sens. 7, 971–989.

Strugnell, N., Lucht, W., Schaaf, C.B., 2001. A global albedo data set derived from AVHRR data for use in climate simulations. Geophys. Res. Lett. 28, 191–194. doi:doi:10.1029/2000GL011580

Tan, B., Woodcock, C.E., Hu, J., Zhang, P., Ozdogan, M., Huang, D., Yang, W., Knyazikhin, Y., Myneni, R.B., 2006. The impact of gridding artifacts on the local spatial properties of MODIS data: Implications for validation, compositing, and band-to-band registration across resolutions. Remote Sens. Environ. 105, 98–114.

Thaiutsa, B., Puangchit, L., Kjelgren, R., Arunpraparut, W., 2008. Urban green space, street tree and heritage large tree assessment in Bangkok, Thailand. Urban For. urban Green. 7, 219–229.

Tomasi, C., Fuzzi, S., Kokhanovsky, A., 2017. Atmospheric Aerosols: Life Cycles and Effects on Air Quality and Climate. John Wiley & Sons.

UNHCR, 2017. Syria Regional Refugee Response - - - Emirati Jordanian Camp (Murijep al Fhoud) [WWW Document]. URL http://data.unhcr.org/syrianrefugees/settlement.php?id=224&country=0&region=0 (accessed 10.25.17).

Vermote, E., Justice, C.O., Csiszar, I., 2014. Early evaluation of the VIIRS calibration, cloud mask and surface reflectance Earth data records. Remote Sens. Environ. 148, 134–145. doi:10.1016/j.rse.2014.03.028

Vermote, E.F., Kotchenova, S., 2008. Atmospheric correction for the monitoring of land surfaces. J. Geophys. Res. 113. doi:doi:10.1029/2007JD009662.

Walther, A., Heidinger, A.K., Miller, S., 2013. The Expected Performance of Cloud Optical and Microphysical Properties derived from Soumi NPP VIIRS Day/Night Band Lunar Reflectance. J. Geophys. Res. Atmos. 2013JD020478. doi:10.1002/2013JD020478

Wang, J., Aegerter, C., Xu, X., Szykman, J.J., 2016. Potential application of VIIRS Day/Night Band for monitoring nighttime surface PM 2.5 air quality from space. Atmos. Environ. 124, 55–63.

Wang, Z., Schaaf, C.B., Strahler, A.H., Chopping, M.J., Román, M.O., Shuai, Y., Woodcock, C.E., Hollinger, D.Y., Fitzjarrald, D.R., 2014. Evaluation of MODIS albedo product (MCD43A) over grassland, agriculture and forest surface types during dormant and snow-covered periods. Remote Sens. Environ. 140, 60–77. doi:10.1016/j.rse.2013.08.025

Wang, Z., Schaaf, C.B., Strahler, A.H., Wang, J., Woodcock, C.E., Chopping, M.J., Román, M.O., Rocha, A. V, Shuai, Y., 2012. Evaluation of Moderate-resolution Imaging Spectroradiometer (MODIS) snow albedo product (MCD43A) over tundra. Remote Sens. Environ. 117, 264–280. doi:doi:10.1016/j.rse.2011.10.002

Wang, Z., Román, M. O., Sun, Q., Molthan, A. L., Schultz, L. A., and Kalb, V. L. (2018). Monitoring Disaster-related Power Outages Using NASA Black Marble Nighttime Light Product. Int. Arch. Photogramm. Remote Sens. Spatial Inf. Sci., XLII-3, 1853-1856, https://doi.org/10.5194/isprs-archives-XLII-3-1853-2018, 2018.

Wang, Z., Shrestha, R. and Román, M. O., (2018). NASA's Black Marble Nighttime Lights Product Suite Algorithm Theoretical Basis Document (ATBD), Version 1.0, April 2018. Available in https://viirsland.gsfc.nasa.gov/PDF/VIIRS_BlackMarble_ATBD_V1.0.pdf.

Wickland, D., Gobron, N., Moore, B., Nakajima, M., Sathyendranath, S., Plummer, S., Schmullius, C., Dubayah, R., 2014. CEOS Strategy for Carbon Observations from Space. 40th COSPAR Sci. Assem. Held 2-10 August 2014, Moscow, Russ. Abstr. A0. 1-2-14. 40, 3626.

WMO, 2016. Observing Systems Capabilities Analysis and Review tool: Rolling Requirements Review process, http://www.wmo.int/pages/prog/www/OSY/RRR-DB.html (accessed 8.25.17).

Wolch, J.R., Byrne, J., Newell, J.P., 2014. Urban green space, public health, and environmental justice: The challenge of making cities "just green enough." Landsc. Urban Plan. 125, 234–244.Wolfe, R.E., Lin, G., Nishihama, M., Tewari, K.P., Tilton, J.C., Isaacman, A.R., 2013. Suomi NPP VIIRS prelaunch and on‐orbit geometric calibration and characterization. J. Geophys. Res. Atmos. 118.

Wolfe, R.E., Nishihama, M., Fleig, A.J., Kuyper, J.A., Roy, D.P., Storey, J.C., Patt, F.S., 2002. Achieving sub-pixel geolocation accuracy in support of MODIS land science. Remote Sens. Environ. 83, 31–49.

Wolfe, R.E., Roy, D.P., Vermote, E., 1998. MODIS land data storage, gridding, and compositing methodology: Level 2 grid. IEEE Trans. Geosci. Remote Sens. 36, 1324–1338.

World Bank, 2017. Rebuilding Infrastructure and Improving Access to Employment in Post Crisis Côte d'Ivoire [WWW Document]. World Bank. URL http://www.worldbank.org/en/results/2016/06/17/rebuilding-infrastructure-and-improving-access-to-employment-in-post-crisis-cote-divoire (accessed 10.24.17).

Xiao, Z., Liang, S., Wang, T., Jiang, B., 2016. Retrieval of Leaf Area Index (LAI) and Fraction of Absorbed Photosynthetically Active Radiation (FAPAR) from VIIRS Time-Series Data. Remote Sens. 8, 351.

Xiong, X., Butler, J., Chiang, K., Efremova, B., Fulbright, J., Lei, N., McIntire, J., Oudrari, H., Sun, J., Wang, Z., 2014. VIIRS on‐orbit calibration methodology and performance. J. Geophys. Res. Atmos. 119, 5065–5078.

Yang, K., Wolfe, R.E., 2001. MODIS level 2 grid with the ISIN map projection, in: Geoscience and Remote Sensing Symposium, 2001. IGARSS'01. IEEE 2001 International. IEEE, pp. 3291–3293.

Yorks, J., Palm, S., McGill, M., Hlavka, D., Hart, W., Selmer, P., Nowottnick, E., 2015. CATS Algorithm Theoretical Basis Document Level 1 and Level 2 Data Products Release 1.

Yorks, J.E., McGill, M.J., Palm, S.P., Hlavka, D.L., Selmer, P.A., Nowottnick, E.P., Vaughan, M.A., Rodier, S.D., Hart, W.D., 2016. An overview of the CATS level 1 processing algorithms and data products. Geophys. Res. Lett. 43, 4632–4639. doi:10.1002/2016GL068006

Yu, B., Shi, K., Hu, Y., Huang, C., Chen, Z., Wu, J., 2015. Poverty evaluation using NPP-VIIRS nighttime light composite data at the county level in China. IEEE J. Sel. Top. Appl. Earth Obs. Remote Sens. 8, 1217–1229. doi:10.1109/JSTARS.2015.2399416

Zhang, Q., Pandey, B., Seto, K.C., 2016. A Robust Method to Generate a Consistent Time Series From DMSP/OLS Nighttime Light Data. IEEE Trans. Geosci. Remote Sens. 54, 5821–5831.

Zhao, F., Strahler, A.H., Schaaf, C., Yao, T., Yang, X., Wang, Z., Schull, M.A., Román, M.O., Woodcock, C.E., Olofsson, P., Ni-Meister, W., Jupp, D.L.B., Lovell, J.L., Culvenor, D.S., Newnham, G.J., 2012. Measuring Gap Fraction, Element Clumping Index and LAI in Sierra Forest Stands Using a Full-waveform Ground-Based Lidar. Remote Sens. Environ. 125, 73–79. doi:doi:10.1016/j.rse.2012.07.007

Zhao, X., Shi, H., Yu, H., Yang, P., 2016. Inversion of Nighttime PM2. 5 Mass Concentration in Beijing Based on the VIIRS Day-Night Band. Atmosphere (Basel). 7, 136.

Appendix A: Metadata (Attributes) in VNP46A1 Product

```
Netcdf VNP46A1_NPP_DNBdailyN.A2016189.h10v05.h5 {
 group: HDFEOS {
  group: ADDITIONAL {
   group: FILE_ATTRIBUTES {
   }
  }

  group: GRIDS {
   group: VNP_Grid_DNB {
    dimensions:
     XDim = 2400;
     YDim = 2400;
     Xdim = 2400;
     Ydim = 2400;
    variables:
     short _HDFEOS_CRS;
      :Projection = "HE5_GCTP_GEO";
      :UpperLeftPointMtrs = -8.0E7, 4.0E7; // double
      :LowerRightMtrs = -7.0E7, 3.0E7; // double

    group: Data_Fields {
     variables:
      float BrightnessTemperature_M12(YDim=2400, XDim=2400);
       :long_name = "Brightness Temperature of band M12 ";
       :units = "Kelvins";

      float BrightnessTemperature_M13(YDim=2400, XDim=2400);
       :long_name = "Brightness Temperature of band M13 ";
       :units = "Kelvins";

      float BrightnessTemperature_M15(YDim=2400, XDim=2400);
       :long_name = "Brightness Temperature of band M15 ";
       :units = "Kelvins";

      float BrightnessTemperature_M16(YDim=2400, XDim=2400);
       :long_name = "Brightness Temperature of band M16 ";
       :units = "Kelvins";

      float DNB_At_Sensor_Radiance_500m(YDim=2400, XDim=2400);
       :long_name = "DNB at Sensor Radiance";
       :units = "nW/(cm2 sr)";

      float Glint_Angle(YDim=2400, XDim=2400);
       :long_name = "Glint Angle";
       :units = "degrees";

      float Granule(YDim=2400, XDim=2400);
       :long_name = "Number of selected Granule";
       :units = "none";

      float Lunar_Azimuth(YDim=2400, XDim=2400);
       :long_name = "Lunar Azimuth Angle";
       :units = "degrees";

      float Lunar_Zenith(YDim=2400, XDim=2400);
       :long_name = "Lunar Zenith Angle";
       :units = "degrees";

      float Moon_Illumination_Fraction(YDim=2400, XDim=2400);
       :long_name = "Moon Illumination Fraction";
       :units = "percentage";

      float Moon_Phase_Angle(YDim=2400, XDim=2400);
       :long_name = "Moon Phase Angle";
       :units = "degrees";

      ushort QF_Cloud_Mask(YDim=2400, XDim=2400);
       :valid_min = 0; // int
       :valid_max = 65534; // int
       :_FillValue = 65535US; // ushort
```

```
        :long_name = "Cloud Mask Status";
        :units = "class flags";
        :flag_meanings = "bit 0: 0=Night, 1=Day\n bits 1-3: Land/Water 000=Land & Desert, 001=Land & no Desert, 010=Inland Water, 011=Sea Water,
101=Coastal\n bits 4-5: Cloud Mask Quality 00=Poor, 01=Low, 10=Medium, 11=High\n bits 6-7: Cloud Confidence 00=Confident Clear, 01=Probably
Clear, 10=Probably Cloudy, 11=Confident Cloudy\n bit 8: Shadow Detected 1=Yes, 0=No\n bit 9: Cirrus Detection (IR) 1=Cloud, 0=No Cloud\n bit 10:
Snow/Ice 1=Snow/Ice, 0=No Snow/Ice\n";

      ushort QF_DNB(YDim=2400, XDim=2400);
        :valid_min = 0; // int
        :valid_max = 65534; // int
        :_FillValue = 65535US; // ushort
        :long_name = "DNB QF";
        :units = "class flags";

      float QF_VIIRS_M10(YDim=2400, XDim=2400);
        :long_name = "Quality Flag of Band M10";
        :units = "class flags";

      float QF_VIIRS_M11(YDim=2400, XDim=2400);
        :long_name = "Quality Flag of Band M11";
        :units = "class flags";

      float QF_VIIRS_M12(YDim=2400, XDim=2400);
        :long_name = "Quality Flag of Band M12";
        :units = "class flags";

      float QF_VIIRS_M13(YDim=2400, XDim=2400);
        :long_name = "Quality Flag of Band M13";
        :units = "class flags";

      float QF_VIIRS_M15(YDim=2400, XDim=2400);
        :long_name = "Quality Flag of Band M15";
        :units = "class flags";

      float QF_VIIRS_M16(YDim=2400, XDim=2400);
        :long_name = "Quality Flag of Band M16";
        :units = "class flags";

      float Radiance_M10(YDim=2400, XDim=2400);
        :long_name = "Band M10 Radiance";
        :units = "W/(m2 micron sr)";

      float Radiance_M11(YDim=2400, XDim=2400);
        :long_name = "Band M11 Radiance";
        :units = "W/(m2 micron sr)";

      float Sensor_Azimuth(YDim=2400, XDim=2400);
        :long_name = "Sensor Azimuth Angle";
        :units = "degrees";

      float Sensor_Zenith(YDim=2400, XDim=2400);
        :long_name = "Sensor Zenith Angle";
        :units = "degrees";

      float Solar_Azimuth(YDim=2400, XDim=2400);
        :long_name = "Solar Azimuth Angle";
        :units = "degrees";

      float Solar_Zenith(YDim=2400, XDim=2400);
        :long_name = "Solar Zenith Angle";
        :units = "degrees";

      float UTC_Time(YDim=2400, XDim=2400);
        :long_name = "View Time (UTC)";
        :units = "decimal hours";

    }

    // group attributes:
    :InputPointer_CM = "NPP_CMN.data.A2016189.h10v05.0654.hdf:NPP_CMN.data.A2016189.h10v05.0700.hdf";
    :InputPointer_L2G_DNB = "NPP_DNBN.data.A2016189.h10v05.0654.hdf:NPP_DNBN.data.A2016189.h10v05.0700.hdf";
    :InputPointer_L2G_Ang = "NPP_DNBN.angles.A2016189.h10v05.0654.hdf:NPP_DNBN.angles.A2016189.h10v05.0700.hdf";
    :InputPointer_L2G_PNTR = "NPP_PTDN.A2016189.h10v05.0654.hdf:NPP_PTDN.A2016189.h10v05.0700.hdf";
```

:InputPointer_DNB =
"../h10v05_2016189/data/NPP_VDNES_L1.A2016189.0654.001.2017168020038.hdf:../h10v05_2016189/data/NPP_VDNES_L1.A2016189.0700.001.2017168004047.hdf";
:InputPointer_Mod = "NPP_MOD.data.A2016189.h10v05.0654.hdf:NPP_MOD.data.A2016189.h10v05.0700.hdf";
:useCM = "No";
:CMfill = "No";
:RangeBeginningDate = "2016-07-07";
:RangeBeginningTime = "00:00:00";
:RangeEndingDate = "2016-07-07";
:RangeEndingTime = "23:59:59";
:NorthBoundingCoord = 40.0; // double
:SouthBoundingCoord = 29.999999999999996; // double
:EastBoundingCoord = -70.0; // double
:WestBoundingCoord = -80.0; // double
:TileID = 61010005; // int
:TileMode = "Night";
:HorizontalTileNumber = 10; // int
:VerticalTileNumber = 5; // int
:NumberofInputGranules = 2; // int
:PGE_Name = "PGE554";
:PGEVersion = "V1.0.1";
:SatelliteInstrument = "NPP_SCI";
:ReprocessingPlanned = "metadata field";
:ReprocessingActual = "metadata field";
:ProcessingEnvironment = "Linux nppdev1";
:ScienceQualityFlagExplanation = "unknown";
}

}

}

group: HDFEOS_INFORMATION {
variables:
char StructMetadata.0(32000);

// group attributes:
:HDFEOSVersion = "HDFEOS_5.1.15";
}

// global attributes:
:featureType = "GRID";
:_CoordSysBuilder = "ucar.nc2.dataset.conv.DefaultConvention";
}

Appendix B: Metadata (Attributes) in VNP46A2 Product

```
netcdf VNP46A2.A2016251.h21v09.h5 {
  group: HDFEOS {
    group: ADDITIONAL {
      group: FILE_ATTRIBUTES {
      }

    }

    group: GRIDS {
      group: VNP_Grid_DNB {
        dimensions:
          XDim = 2400;
          YDim = 2400;
        variables:
          short _HDFEOS_CRS;
            :Projection = "HE5_GCTP_GEO";
            :UpperLeftPointMtrs = 3.0E7, 0.0; // double
            :LowerRightMtrs = 4.0E7, -1.0E7; // double

        group: Data_Fields {
          variables:
            double DNB_BRDF-CORRECTED_NTL_500m(YDim=2400, XDim=2400);
              :long_name = "BRDF Corrected DNB Radiance \n";
              :units = "nWatts/(cm^2·sr) \n";
              :valid_range = "0-65534 \n";
              :offset = 0.0; // double
              :_ChunkSizes = 100U, 2400U; // uint

            double DNB_Lunar_Irradiance(YDim=2400, XDim=2400);
              :long_name = "Lunar Irradiance \n";
              :units = "nWatts/(cm^2) \n";
              :valid_range = "0-65534 \n";
              :offset = 0.0; // double
              :_ChunkSizes = 100U, 2400U; // uint

            double Latest_High_Quality_Retrieval(YDim=2400, XDim=2400);
              :long_name = "The Latest High Quality BRDF Corrected DNB Radiance Retrieval\n";
              :units = "Number of Days \n";
              :valid_range = "0 - 254 \n";
              :offset = 0.0; // double
              :_ChunkSizes = 100U, 2400U; // uint

            ubyte Mandatory_Quality_Flag(YDim=2400, XDim=2400);
              :long_name = "Mandatory Quality Flag of BRDF Corrected DNB Radiance \n";
              :units = "nWatts/(cm^2";
              :valid_range = "0 - 3 \n";
              :Description = "00\tHigh-Quality\tMain Algorithm (Persistent Nighttime Lights)\n01\tHigh-Quality\tMain Algorithm (Ephemeral Nighttime
Lights)\n02\tGood-Quality\tBack up Algorithm (Temporal Gap-Filling)\n03\tPoor-Quality\tMain Algorithm (Outlier, potential cloud contamination or
other issues)\n255\tNo Retrieval\tFill Value \n";
              :_FillValue = 255UB; // ubyte
              :_ChunkSizes = 100U, 2400U; // uint

            ushort QF_Cloud_Mask(YDim=2400, XDim=2400);
              :long_name = "Cloud Mask Status \n";
              :units = "class flag \n";
              :valid_range = "0 - 65534 \n";
              :Description = "bit     Flag description key: \n0\t    Day/Night \n       0=Night  1=Day \n1-3\t    Land/Water Background \n\t\t000=Land & Desert
\n\t\t001=Land no Desert \n\t\t010=Inland Water \n\t\t011=Sea Water \n\t\t101=Coastal \n4-5\t    Cloud Mask Quality \n\t\t00=Poor\n\t\t01=Low
\n\t\t10=Medium \n\t\t11=High \n6-7\t    Cloud Detection Results & Confidence Indicator \n\t\t00=Confident Clear \n\t\t01=Probably Clear
\n\t\t10=Probably Cloudy \n\t\t11=Confident Cloudy \n8\t    Shadow Detected \n\t\t1=Yes   0=No \n9\t    Cirrus Detection (IR) (BTM15-BTM16)
\n\t\t1=Cloud  0=No Cloud \n";
              :_FillValue = 65535US; // ushort
              :_ChunkSizes = 100U, 2400U; // uint

            ubyte Snow_Flag(YDim=2400, XDim=2400);
              :long_name = "Snow/Ice Status \n";
              :units = "class flag \n";
              :valid_range = "0 - 1 \n";
              :Description = "0 = No snow/ice \n  1 = snow/ice \n";
              :_FillValue = 255UB; // ubyte
```

```
            :_ChunkSizes = 100U, 2400U; // uint

        }

      }

    }

  }

  group: HDFEOS_INFORMATION {
    variables:
      char StructMetadata.0(32000);

    // group attributes:
    :HDFEOSVersion = "HDFEOS_5.1.15";
  }

  // global attributes:
  :featureType = "GRID";
  :_CoordSysBuilder = "ucar.nc2.dataset.conv.DefaultConvention";
}
```